

# Anisotropic magnetoresistance: materials, models and applications

Philipp Ritzinger<sup>1,2</sup> and Karel Výborný<sup>1</sup>

<sup>1</sup>*FZU — Institute of Physics, Academy of Sciences of the Czech Republic,  
Cukrovarnická 10, Praha 6, CZ-16253*

<sup>2</sup>*MFf — Faculty of Mathematics and Physics, Charles University,  
Ke Karlovu 5, Praha 2, CZ-12000\**

## Abstract

Resistance of certain (conductive and otherwise isotropic) ferromagnets turns out to exhibit anisotropy with respect to the direction magnetisation:  $R_{\parallel}$  different from  $R_{\perp}$  with reference to the electric current direction. This century-old phenomenon is reviewed both from the perspective of materials and physical mechanisms involved. More recently, this effect has also been extended to antiferromagnets. This opens the possibility for industrial applications reaching far beyond the current ones, e.g. hard drive read heads.

## I. INTRO

Electric resistance  $R$  of a conductor depends on the state of its magnetic order; for example, in ferromagnetic metals at saturation, it depends on the direction of magnetisation  $\vec{M}$ . Experimentally, control of external magnetic field  $\vec{B}$  allows to change  $\vec{M}$  and this suggests the name *magnetoresistance*. The reader should not be misled into thinking that any dependence  $R(B)$  is confined to magnetically ordered materials though. Magnetoresistances encompass a wide range of phenomena and in this review, we only focus on situations where the *anisotropy* of  $R$  is caused by magnetic order. By large part, we will discuss ferromagnets (FMs) where such anisotropic magnetoresistance (AMR) has been explored extensively but only few reviews exist and the most popular Potter and McGuire<sup>1</sup> article is now almost half a century old. More modern developments of the field will also be discussed where as there seems to be a shift of focus from FMs to materials with more complex magnetic order (of which antiferromagnets are of particular interest) and here, even an elementary consensus on terminology is still to be reached.

After this introductory Section, we turn our attention to approaches to model and thus understand the AMR on phenomenological and microscopic level (Sec. 2) and then, to materials where AMR has been explored (Sec. 3). AMR applications are discussed in Sec. 4 and the last section is devoted to conclusions.

### A. Basic observations

The basic approach to quantify AMR in a given ferromagnetic material is to compare resistance for magnetisation parallel and perpendicular to current direction relative<sup>2</sup> to their suitably chosen average  $R_0$ :

$$\text{AMR} = \frac{R_{\parallel} - R_{\perp}}{R_0}. \quad (1)$$

Depending on context, the most obvious choice  $R_0 = (R_{\parallel} + R_{\perp})/2$  may be replaced by another weighted sum<sup>1</sup> but since AMR is typically of the order of per cent, this is usually of little consequence. AMR in most metals is positive and it depends on temperature: it vanishes when magnetic order is lost upon heating.

A more careful analysis of AMR requires the consideration of full resistivity tensor  $\rho_{ij}$ . In a single crystal (of sufficiently low<sup>210</sup> symmetry), anisotropies appear already for  $\vec{M} = 0$  and

the AMR must not be confused with these 'fundamental anisotropies'. Even cubic systems can, however, exhibit non-zero off-diagonal components of  $\rho_{ij}$  under non-zero magnetisation (see Sec. 1c) and to this end, angular dependence of  $\rho$  should be considered; the most common observation is

$$\rho_{xx}/\rho_0 = 1 + C_I \cos 2\varphi \quad (2)$$

where  $C_I$  is sometimes called non-crystalline AMR because it survives (as opposed to the more complex angular dependences discussed in Sec. III A for example) even in polycrystalline systems. Eq. 2 can be obtained by averaging expressions such as Eq. 11 over orientations of crystallites whereupon only  $\varphi$  (angle between current and  $\vec{M}$ ) remains invariant. Clearly the AMR as defined in Eq. 1 is just twice  $C_I$  when no crystalline AMR is present.

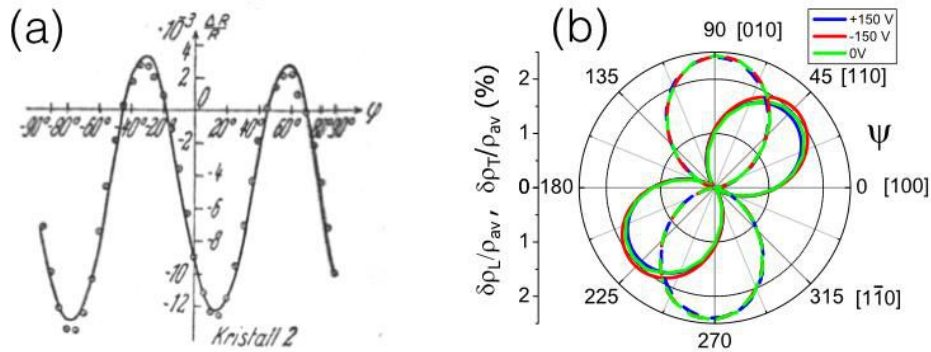


FIG. 1: Two basic examples of AMR measurement. (a) Dörings measurements on nickel crystals, (b) longitudinal and transversal AMR measured on (Ga,Mn)As thin films. Reproduced from (a) Ref.<sup>5</sup> and (b) Ref.<sup>6</sup>.

## B. History and More Features

*Discovery.* Transition metals were the first materials where AMR was discovered: in 1857, William Thomson measured<sup>3</sup> in Fe and Ni what we would call non-crystalline AMR nowadays. The discovery in the third elemental room temperature ferromagnet, Co, was made a little later<sup>4</sup> While these measurements concerned polycrystalline samples, Döring in 1938 investigated<sup>5</sup> the AMR in Fe and Ni single-crystals more thoroughly as a function of  $\varphi$  and also the angle of  $\vec{M}$  respective to crystallographic directions. Apart from the

non-crystalline AMR (2) terms dependent on crystal symmetry (crystalline AMR) were found. His phenomenological approach to describe the full AMR in single crystals is still frequently used in modern works<sup>6–10</sup> as discussed in sec. III A.

*Intrinsic and Extrinsic AMR.* Next to the possible classification into non-crystalline and crystalline AMR, we can also make the distinction between intrinsic and extrinsic contributions. In the simplest case of Drude formula,

$$\sigma_0 = \frac{ne^2\tau}{m} = \omega_p^2\epsilon\tau, \quad \sigma(\omega) = \frac{\sigma_0}{1 - i\omega\tau} \quad (3)$$

the extrinsic (thus scattering-dependent) effects enter through the the dependence of relaxation time  $\tau$  on the magnetisation direction while the intrinsic contribution to AMR amounts to such a dependence of the plasma frequency  $\omega_p$ . Examples of the former mechanism can be captured by effective models described in Sec. 2(b)i and the prime example is s-d-scattering, thus, that delocalized conduction electrons (4s) are scattering into localized 3d states via magnetic impurities. Intrinsic AMR receives more attention in recent years<sup>11</sup>, since investigated materials are generally more complicated and bandstructure-calculation has become more precise, allowing for a more thorough distinction. On a theoretical side, AMR can be calculated from the bandstructure (intrinsic contribution) and is then compared to experimental results. If there happens to be a significant difference, this can be attributed to scattering (extrinsic contribution). Experimentally, the usage of AC-voltage can be used to distinguish<sup>12</sup> the intrinsic and extrinsic contributions to  $\sigma(\omega)$  in Eq. (3), since the intrinsic contribution leads to frequency-independent term in AMR, while the extrinsic contribution scales with  $\propto 1/\omega$ , see Sec. 4(b)i for details.

*Negative AMR.* In most common metals, AMR as defined by Eq. (1) is positive; this is fairly demonstrated by Tab. I which shows also one of early examples of systems where AMR is negative (cobalt with traces of iridium). The first materials where negative AMR was found were, nevertheless, much more common alloys of transition metals with aluminium<sup>13</sup>. The belief that negative AMR is an exception established itself in the next couple of decades, which may be fueled by the fact that major theories of AMR were developed on simple transition metals showing positive AMR under normal circumstances.

One of the main approaches to microscopically understand the AMR, so called *sd*-model

which is explained in Sec. 2(b)i, allows to understand the AMR sign (in some materials) using the following simplified picture based on Mott's two-current model<sup>14</sup> which operates with two spin channels and their resistivities  $\rho_{\uparrow,\downarrow}$ . We will follow explanations by Kokado, Tsunoda et al.<sup>15</sup>, where the DOS at Fermi level  $E_F$  in the majority/minority  $d$ -bands is  $d_{\uparrow}/d_{\downarrow}$ . As Fig. 2 shows, majority spin conduction (hence  $d_{\uparrow} > d_{\downarrow}$  and  $\rho_{\uparrow} > \rho_{\downarrow}$  and vice versa) is responsible positive AMR, while minority spin conduction ( $d_{\uparrow} < d_{\downarrow}$  and  $\rho_{\uparrow} > \rho_{\downarrow}$  and vice versa) causes negative AMR. The key parameter is thus  $\alpha = \rho_{\downarrow}/\rho_{\uparrow}$  and a detailed discussion<sup>15</sup> serves as a useful guideline for the AMR sign across the whole material class of transition metals. Validity of this guideline is limited, however, by the range of applicability of the  $sd$ -model: other material classes, such as dilute magnetic semiconductors discussed in Sec.3(b), follow different patterns<sup>16,17</sup>.

In the context of this theory<sup>15</sup>, negative AMR is sometimes promoted to be a possible sign of half-metallicity<sup>18-20</sup>, which has to be taken with caution: first, the sign of AMR as defined by Eq. (1) may depend on the current direction with respect to the crystal (in which case it makes better sense to analyse AMR in terms of its non-crystalline and crystalline components, *see Sec. 2a*) and this clearly cannot mean that the system would be half-metal in one case and normal metal in the other case. An example of a material which is clearly *not* a half-metal is the 30:70 alloy of iron and cobalt<sup>21</sup> (sign change of AMR can be seen in Fig. 2 of that reference where  $\vec{B}$  and  $\vec{M}$  are nearly parallel). Also, temperature variation can cause similar changes (e.g. in  $\text{Mn}_4\text{N}$ <sup>22</sup>). Second even in predominantly negative signed Co-based Heusler alloys, positive AMR was reported by e.g. variations of the stoichiometry<sup>20</sup> or the annealing temperature<sup>23</sup> (see sec. III D). The changes of sign in all of these materials were explained successfully within the framework of the aforementioned majority/minority scattering by Kokado and Tsunoda.

	$\rho_{\downarrow} > \rho_{\uparrow}$	$\rho_{\uparrow} > \rho_{\downarrow}$
$d_{\uparrow} > d_{\downarrow}$	(c) neg.	(a) pos.
$d_{\uparrow} < d_{\downarrow}$	(b) pos.	(d) neg.

FIG. 2: Sign of AMR explained in the context of  $sd$  model. Examples: (a) bcc Fe, (b) fcc Co or Ni, (c) half-metallic ferromagnets such as  $\text{Co}_2\text{MnAl}_{1-x}\text{Si}_x$ , and (d)  $\text{Fe}_4\text{N}$ . Inspired heavily by Fig. 4 of Kokado et al.<sup>15</sup>.

Still, it holds true that half-metallic density of states induces negative sign of AMR. The backwards conclusion (negative sign implies half-metallicity<sup>21</sup>) is not generally true. Other systems where AMR can be negative will be discussed later throughout this review: certain antiferromagnets, manganites, two-dimensional electron gases to name a few.

### C. AMR and the more fancy effects

We first wish to elucidate the relationship of AMR to off-diagonal component of the resistivity tensor,

$$\rho_{xy}/\rho_0 = C_I \sin 2\varphi \quad (4)$$

in the simplest case, which is often called the planar Hall effect. Assume a planar system with magnetization  $\vec{m} \parallel x$  which would be otherwise isotropic (in other words,  $\vec{m}$  provides the only source of symmetry breaking). Let us denote the two non-zero components  $\rho_{xx}$  and  $\rho_{yy}$  by  $\rho_{\parallel}$  and  $\rho_{\perp}$ , respectively. Now consider a rotation of  $\vec{m}$  to  $R_{\phi}\vec{m}$ : in a polycrystal, this would be equivalent to leaving  $\vec{m}$  unchanged and rotating the resistivity tensor instead:

$$R_{\phi} \begin{pmatrix} \rho_{\parallel} & 0 \\ 0 & \rho_{\perp} \end{pmatrix} R_{\phi}^T = \begin{pmatrix} \rho_0 + \frac{1}{2}\Delta\rho \cos 2\phi & \frac{1}{2}\Delta\rho \sin 2\phi \\ \frac{1}{2}\Delta\rho \sin 2\phi & \rho_0 - \frac{1}{2}\Delta\rho \cos 2\phi \end{pmatrix} \quad (5)$$

where  $\Delta\rho = \rho_{\parallel} - \rho_{\perp}$  and  $R_{\phi}$  is an orthogonal matrix. The off-diagonal elements can be identified with Eq. (4) and it is therefore appropriate to call that effect (i.e. PHE) the transversal AMR. As a remark we point out that 'transverse AMR' is sometimes used<sup>24</sup> to describe the experimental configuration where magnetisation rotates in the plane perpendicular to the current direction (*green curve* shown in Fig. 3); in Eqs. (2, 4) this corresponds to constant  $\phi = \pi/2$  and one would then naively expect no variation of resistance. We explain in Sec. 2(a) that *crystalline AMR* is responsible for any signal measured in this setup.

AMR belongs to a wider family of transport phenomena in magnetically ordered materials and in the following we mention several further examples of its members. They are all bound by Onsager reciprocity relations, for resistivity tensor they read

$$\rho_{ij}(M, B) = \rho_{ji}(-M, -B) \quad (6)$$

and to begin with, we observe that for  $\rho_{xy}$ , this relation can be fulfilled either by Eq. (4) in the transverse AMR (a symmetric tensor component  $\rho_{xy} = \rho_{yx}$  which is even in magnetisation)

or by the anomalous Hall effect (AHE) with  $\rho_{xy} = -\rho_{yx}$  odd in magnetisation. Next, there are thermoelectric counterparts of these effects, the anomalous Nernst effect (to AHE) and the anisotropic magnetothermopower discussed in Sec. 4(b)iii. Spin conductivity instead of charge conductivity can also be studied (e.g. SHE instead of AHE) and both effects are closely related<sup>25</sup>, e.g. in permalloy AHE scales with the spin Hall effect (SHE) in proportion to the spin polarisation. Finally, we wish to mention transport in ballistic rather than diffusive regime: tunneling AMR (TAMR) and ballistic AMR discussed in Sec. 4(b)iv.

#### D. What is AMR and what it is not

Magnetoresistance (MR) may refer to any phenomenon<sup>26</sup> where  $R(B)$  is not constant and as such they are not limited in scope to magnetically ordered materials. Orbital effects leading to MR imprint the anisotropy of crystal to  $R(B)$ , as recently nicely reviewed by Zhang et al.<sup>27</sup>, and ensuing anisotropic MR is *not* the subject of the present review.

On the other hand, the AMR appears under different names in literature: spontaneous magnetoresistance anisotropy (SMA)<sup>28</sup>, spontaneous resistivity anisotropy (SRA)<sup>29,30</sup>, ferromagnetic anisotropy of resistivity (FAR)<sup>31</sup> or magneto-resistivity anisotropy<sup>32</sup>. Also, longitudinal MR and transversal MR are sometimes discussed separately<sup>33</sup> whereas their difference in high magnetic field is the actual AMR. In some occasions, the term AMR or anisotropic MR is used, when the MR ratio is plotted for different field directions<sup>34,35</sup>. In that case it can be, that the AMR ratio is not quantitatively calculated as in Eq. 1, but the discussion is rather restricted to the mere fact, that the MR is different for different field direction, thus implying AMR. Ideally, we are interested in magnetically ordered materials at saturation.

*Misconception with MCA.* A frequent trouble is the confusion of AMR and magneto-crystalline Anisotropy (MCA). Whenever there is a deviation from the classical two-fold dependence  $\Delta\rho \propto \cos^2(\angle(\mathbf{H}, \mathbf{J}))$  (where  $\mathbf{H}$  and  $\mathbf{J}$  is the current density) it is not per se clear whether they stem from MCA or are AMR terms. MCA can lead to higher-order symmetries on the AMR signal, however these terms might also origin from AMR due to crystalline symmetry (so called *crystalline AMR* or *single-crystal AMR* (SCAMR)). The frequent conclusion, the higher-order terms are stemming from MCA is only unequivocally

true in polycrystalline materials. In single-crystals a careful distinction of these MCA and AMR is always mandatory (e.g. by determining the value of MCA in a different experiment and account for it). Furthermore it should be kept in mind that crystalline AMR and MCA are not the same effect: While both are dependent on the bandstructure, a key ingredient of any (extrinsic) AMR is scattering, which does not play a role in MCA. The intrinsic AMR depends on the anisotropy of the fermi velocities, which is not necessarily linked to the exchange energy causing the MCA into existence. The concept of MCA is further elaborated in section IE and the crystalline AMR is derived and explained in detail in section III A. An illustration of the difference of AMR and MCA can be seen in Fig. 4d-g of<sup>32</sup>, where the AMR and MCA show much different temperature dependences.

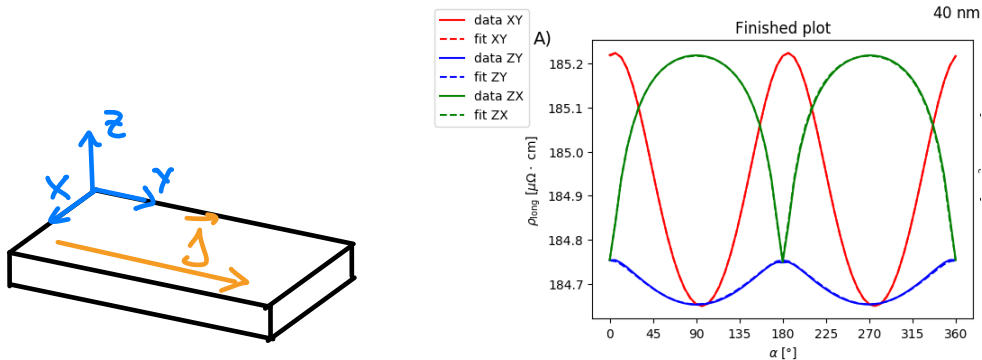


FIG. 3: Example of Stoner-Wohlfarth analysis in AMR data of a  $\text{Co}_2\text{MnGa}$  thin-film sample. Alongside the SW1 model and a basic non-crystalline AMR, also higher-order crystalline AMR terms are taken into account (see sec. II A). There is an excellent agreement between data and fit. The magnetic field was rotated in three different rotation planes denoted as XY, ZY and ZX, where  $Z = \hat{n} \parallel [001]$ ,  $Y = \hat{j} \parallel [110]$  and  $X = Y \times Z$ . The rotation in the XY plane begins at the X axis and in the other plane at the Z axis. Reproduced from Ref.<sup>44</sup>.

### E. Step one: magnetisation control

As already explained, it is usually the applied magnetic field  $\vec{B}$  that steers the magnetic moments. In other words, it is desirable to determine the magnetic state depending on  $\vec{B}$ . First, we assume that we are looking at a single-domain state (effects related to a non-trivial domain structure tend to be more severe in antiferromagnets<sup>36</sup>); next, we want to focus only on classical magnetism. Under these assumptions we are basically left with

inter-sublattice exchange coupling (if there's more than just one magnetic sublattice) and magnetic anisotropy.

A convenient framework in ferromagnets is the time-proven Stoner-Wohlfarth model<sup>37</sup> (henceforth referred to as the SW1 model), summarised by Eq. 2 in<sup>38</sup>, which yields the local energy minimum for magnetisation depending on history and two parameters:  $B = |\vec{B}|$  and  $B_a$  (magnetic anisotropy). Among others, SW1 models are widely used in the analysis of resistivity data. An example can be found in Fig. 3, where next to basic non-crystalline AMR, a SW1 model and higher order crystalline AMR components were taken into account (see Sec2(a) for the latter); the latter become manifest in (a) the different amplitudes of the blue and red curves or (b) non-constant signal plotted as the green curve. As for (b), magnetisation remains always perpendicular to current,  $\varphi = \pi/2$ , and if Eq. (2) were the complete description of AMR in this case,  $\rho_{yy}$  should remain constant. By including *crystalline AMR* terms into Eq. (2) as discussed later, see Eq. (11), the observed behaviour both for (b) and (a) can be well understood. The same type of description (based on SW1, see Fig. 8) was used by Limmer et al<sup>8,39</sup> for (Ga,Mn)As.

As soon as there are more than one magnetic sublattice (MSL), the situation becomes less straightforward<sup>40</sup>. It is possible to generalise the previous approach to antiferromagnets with two MSLs: such SW2 model reads

$$\frac{E}{MV} = B_e \vec{m}_1 \cdot \vec{m}_2 - B \vec{b} \cdot (\vec{m}_1 + \vec{m}_2) + B_a [(\vec{m}_1 \cdot \hat{a})^2 + (\vec{m}_2 \cdot \hat{a})^2]. \quad (7)$$

and a new parameter has been introduced: the inter-sublattice exchange coupling  $B_e$ . The basic mode of operation of SW2<sup>41</sup> is that the Néel vector  $\vec{L} = \vec{m}_1 - \vec{m}_2$  is perpendicular to  $\vec{B}$  which always (for  $|B| > 0$ ) corresponds to energy minimum in Eq. (7) once  $B_a = 0$ . In this way,  $\vec{L}$  can be effectively controlled by  $\vec{B}$  and for finite  $B_a$ , the same applies beyond spin-flop field  $\propto \sqrt{B_a B_e}$ .

This concept can be extended to more complicated systems and starting with SW3, non-collinear magnetic order has to be considered. Recently,  $Mn_3X$  materials (where X can be Ge or Sn, for example) attracted significant attention and Liu and Balents<sup>42</sup> discuss a model where beyond adding a third MSL to Eq. (7) also Dzyaloshinskii-Moriya interaction is included. Geometry of kagome lattice (see Fig. 16) introduces frustration and relationships between  $\vec{B}$  and  $\vec{m}_{1,2,3}$  are in general difficult to describe in simple terms.

## II. MODELLING

In this chapter, the different modelling approaches are presented. We will start in sec. IIA by introducing potent phenomenological models, which allow to effectively analyse the even most complex AMR data. Due to their phenomenological nature, however, they cannot give insight about the possible origins of individual terms in expansions such as (11). While more involved, microscopical models reviewed in Sec. IIB make such deeper understanding possible.

### A. Phenomenological models

We define the magnetic field direction to be  $\mathbf{h} = \mathbf{H}/H$  and the magnetization direction to be  $\mathbf{m} = \mathbf{M}/M$ . Please keep in mind that the AMR depends on  $\mathbf{m}$  and not on  $\mathbf{h}$  - the rotation of the magnetic field is simply used to control the rotation of the magnetization. The dependence of  $\mathbf{m}$  on  $\mathbf{h}$  was discussed in the previous section and the confusion of MCA with AMR in sec. ID. Broadly speaking it holds that:  $AMR = \rho(\mathbf{m}) \neq \rho(\mathbf{h})$ .

The simplest possible way to describe the AMR presents itself as (2):  $\Delta\rho(\mathbf{m}) \propto \cos(2\varphi)$ , where  $\varphi$  is the angle between  $\mathbf{m}$  and current direction  $\mathbf{j} = \mathbf{J}/J$ . In a single-crystal this simple picture does not hold anymore, but instead the AMR can have more complex contributions depending on the crystalline symmetry. In the following section, we will present a simple yet extremely powerful phenomenological model to describe (however *not* explain) even complex AMR data, which was originally developed by Döring in 1938<sup>5</sup> and since then used many times again<sup>6-10,39</sup>.

*The model.* To begin with, we assume that we do not know the correct analytical expression of the resistivity  $\rho$  and that  $\rho$  depends only on the direction of the magnetization  $\mathbf{m}$ . Furthermore, there can be higher-order dependencies on  $\mathbf{m}$ . Thus, we express  $\rho$  as a power series of  $\mathbf{m}$ :

$$\rho_{ij}(\hat{m}) = \rho_{ij}^{(0)} + \rho_{ijk}^{(1)} m_k + \rho_{ijkl}^{(2)} m_k m_l + \rho_{ijklm}^{(3)} m_k m_l m_m + \rho_{ijklmn}^{(4)} m_k m_l m_m m_n + \dots \quad (8)$$

where  $\rho_{ij}^{(0)}$ ,  $\rho_{ijk}^{(1)}$ ,  $\rho_{ijkl}^{(2)}$ ,  $\rho_{ijklm}^{(3)}$  and  $\rho_{ijklmn}^{(4)}$  are the expansion coefficients and  $m_k, m_l, m_m, m_n \in \{m_{[100]}, m_{[010]}, m_{[001]}\}$  are the cartesian components of  $\mathbf{m}$ .

The number of independent parameters is reduced by using the following four strategies: (i) Commutation  $m_k m_l = m_l m_k$  for all  $m_k$  and  $m_l$ , (ii) the identity  $\mathbf{m}^2 = \sum_k m_k^2 = 1$ , (iii) the Onsager relation<sup>7</sup>:  $\rho_{ij}(\hat{m}) = \rho_{ji}(-\hat{m})$  and (iv) Neumann's principle: The resistivity tensor, as well as its expansion coefficients, must reflect the crystal symmetry<sup>43</sup>. There are several ways to account for the symmetry, e.g. by using generator matrices of the crystal symmetries is shown in<sup>7,8,39</sup>.

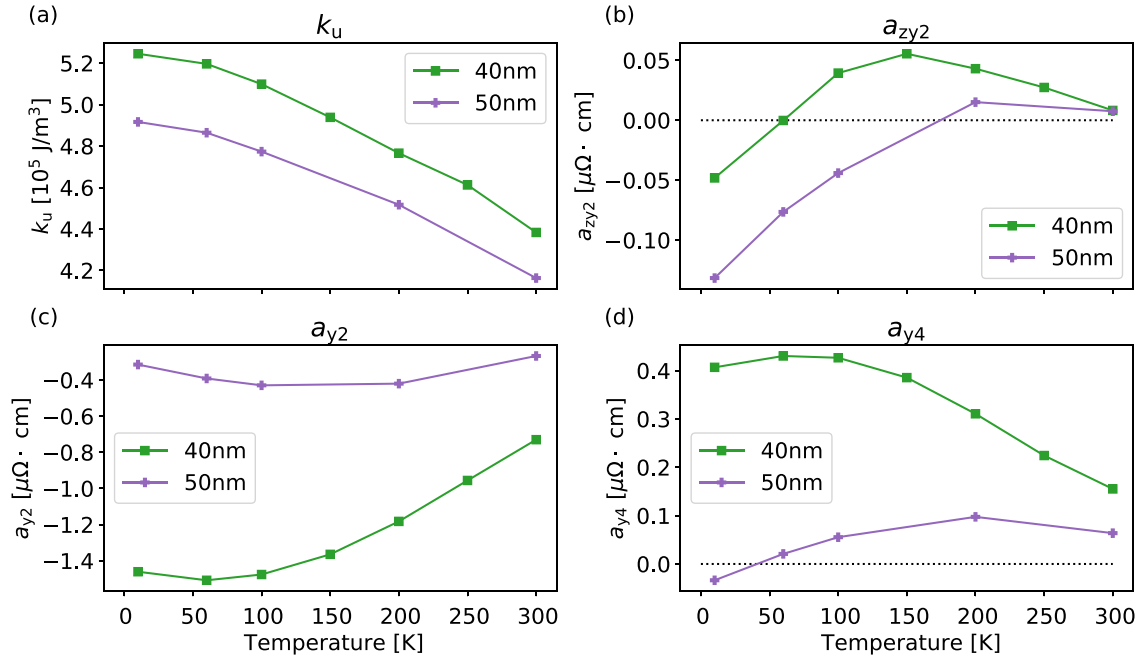


FIG. 4: Temperature evolution of the phenomenological parameters obtained by the fit to AMR data of two Co<sub>2</sub>MnGa thin-film samples. (a) Uniaxial magnetic anisotropy from the SW1 model and (b–d) part of the parameters for AMR in tetragonal symmetry similar to those defined in Eq. 10. Reproduced from Ref.<sup>10</sup>.

For a more detailed treatment it can be wise to consider the previously mentioned publications, especially the treatment in<sup>7</sup>. Next, we explain how the great number of coefficients appearing in Eq. (8) can be reduced to a small set of key parameters such as those shown

in Fig. 4 for a specific tetragonal system.

Please note, that this approach yields an expression for the resistivity tensor  $\rho_{ij}$  differing depending on the crystal symmetry. The tensor in cubic symmetry can (among others) be found in Eq. 4 of<sup>39</sup> and in tetragonal symmetry in Eq. 4 and 5 of<sup>39</sup>. The resulting tensor depends generally on the components  $m_k$  of  $\mathbf{m}$  and also on coefficients  $A, B, \dots$  which are unknown in the general case and are sample-dependent.

The longitudinal resistivity  $\rho$  is obtained by applying Ohm's law:  $\rho = \mathbf{j}\rho_{ij}\mathbf{j}$ . The coefficients of the resistivity do change depending on the crystal symmetry and on the current direction. As an example,  $\rho$  in cubic symmetry with  $\mathbf{j} \parallel [100] \equiv j_x$  writes as:

$$\rho = \rho_0 + a_{x2} \cdot m_x^2 + a_{x4} \cdot m_x^4 + a_{zy2} \cdot m_z^2 \cdot m_y^2 \quad (9)$$

$$= \rho_0 + a_{x2} \cos(\phi)^2 \sin(\theta)^2 + a_{x4} \cos(\phi)^4 \sin(\theta)^4 + a_{zy2} \sin(\phi)^2 \sin(\theta)^2 \cos(\theta)^2 \quad (10)$$

where the  $a_{x2}, a_{x4}, a_{zy2}$  are effective sample-dependent coefficients, which are linked to the original set of coefficients  $A, B, \dots$  and in the second step a parametrization of  $\mathbf{m}$  in polar coordinates  $\mathbf{m} = (\cos(\phi) \sin(\theta), \sin(\phi) \sin(\theta), \cos(\theta))$  was applied. The calculations are lengthy and can be found elsewhere, alongside with expressions for the longitudinal resistivity for current along [110] or the resistivity tensor for tetragonal crystal symmetry<sup>7,8,10,39</sup>. Expressions for other symmetries in literature are not known to us. Please note, that the same approach is valid in order to investigate transversal resistivity, thus Hall effect. An example for the temperature evolution of some of these phenomenological coefficients in two  $\text{Co}_2\text{MnGa}$  thin-film samples with tetragonal symmetry can be found in Fig. 4.

Eq. 10 is only one possible way of writing things down. For example, Döring<sup>5</sup> expresses the resistivity in terms of direction cosines of the magnetization  $\alpha_i$  and of the current  $\beta_i$ . Another way of describing the AMR is given by<sup>6</sup>:

$$\frac{\Delta\rho_{\text{long}}}{\rho_{\text{av}}} = \underbrace{C_I \cdot \cos(2\varphi)}_{\text{non-crystalline}} + \overbrace{C_U \cdot \cos(2\psi)}^{\text{uniaxial crystalline}} + \underbrace{C_C \cdot \cos(4\psi)}_{\text{cubic crystalline}} + \overbrace{C_{IC} \cdot \cos(4\psi - 2\varphi)}^{\text{mixed non-crystalline/crystalline}} \quad (11)$$

where  $\varphi$  is the angle between  $\mathbf{m}$  and  $\mathbf{j}$  and  $\psi$  is the angle between  $\mathbf{m}$  and a certain, fixed crystallographic direction in the plane of rotation. Eq. 11 is consistent with the previously shown ansatz Eq. 10, which was shown in<sup>44</sup>. However Eq. 11 is only a two-dimensional

equation ( $\mathbf{m}$  rotated in the plane of the surface), while Eq. 10 is a three-dimensional equation (AMR can be described for arbitrary  $\mathbf{m}$  on a spherical surface via  $\phi$  and  $\theta$ . In all cases saturation is implied, thus the length of  $\mathbf{M}$  is irrelevant.) The usage of two angles  $\phi$  and  $\psi$  is slightly confusing since it implies three-dimensionality, however  $\phi$  and  $\psi$  are not defined with respect to different spatial dimensions but instead to different reference axis in order to distinguish between the so-called crystalline and non-crystalline case.

*Higher-order contributions* are due to crystal structure and thus only appearing in single-crystals or epitaxial materials with sufficient crystal quality. In polycrystalline materials, the AMR will be two-fold (see Eq. 2) as can be shown by theoretically by averaging the resistivity tensor over all possible crystal orientations (see<sup>7,8,39</sup>) - or even simpler, to set  $\psi \equiv 0$  in Eq. 11 since crystalline directions do not have any meaning in the polycrystalline limit. In doing so one will recover Eq. 2. This emphasises the usage of the terms non-crystalline (= independent of crystal structure and thus two-fold) and crystalline AMR.

The origin of the crystalline AMR is still under active investigation. While many studies restrict themselves to the mere existence of e.g. a four-fold symmetry, the picture is more complex since the AMR consists of many contributions in various crystalline direction as can be seen above (and e.g. in<sup>5,7-10,39</sup>). While these studies are an accurate description of all the terms possibly existing in the AMR, microscopic studies are rare. For the case of a four-fold symmetry, the effective model of Kokado and Tsunoda<sup>45</sup> (and see following section) showed that a tetragonal symmetry is needed for the four-fold term to appear. The appearance of four-fold terms in many technically cubic materials can be linked to tetragonal distortions induced to thin-films by many substrates.

However, a study describing all the terms in Eq. 10 as well a study for even higher order terms, is still missing to date.

While relatively rare, higher order crystalline terms have also been reported. In hexagonal crystal structures, six-fold AMR can emerge. This was reported for instance in antiferromagnetic MnTe<sup>46</sup>, but also in two-dimensional electron gases on hexagonal [111] interfaces between transition-metal oxides as discussed further in Sec. 3(e). The highest symmetry reported is a eight-fold symmetry measured in (Ga,Mn)As<sup>47</sup> and in (In,Fe)As<sup>48</sup>. In the latter case it was explained by crystal field effects due to a zinc-blende structure.

## B. Microscopic models

Regardless of the detailed structure of a microscopic model aiming to describe AMR in a particular material, two basic ingredients are needed: reasonably accurate knowledge of the electronic structure and that of momentum relaxation. On the level of Eq. 3, this was reduced to the plasma frequency which can be evaluated, see Sec. 2b(i), from electron dispersion  $E_{\vec{k}}$

$$\omega_p^2 = 8\pi^2 \hbar^2 e^2 \int \frac{d^3k}{(2\pi)^2} v_x^2 \delta(E_{\vec{k}} - E_F) \quad (12)$$

and, regarding the momentum relaxation, to transport relaxation time which can be accessed through the Fermi golden rule

$$\frac{1}{\tau} = \frac{2\pi n_{imp}}{\hbar} \int dk' \delta(E_i - E_f) |M_{kk'}|^2 (1 - \cos \theta_{kk'}) \quad (13)$$

whereas we only consider scattering on static disorder (such as point defects in crystal with density  $n_{imp}$ ). In the following, we elaborate on two possible strategies to treat both these ingredients and even if Eqs. (12,13) represent only *examples* of how electronic structure and scattering can be taken into account, any microscopic model of AMR must in some way consider them both. We proceed to explain effective models whereas symbols appearing in the preceding equations will also be described. Our focus will be, in general, on systems with metallic conduction and other situations (such as hopping conduction or systems with bound magnetic polarons<sup>49</sup>) will not be discussed in this review.

### 1. Effective models

Most transport phenomena depend on band structure solely in the vicinity of Fermi level<sup>50</sup>  $E_F$ . To that end, integral in Eq. 12 needs only limited knowledge of band structure (and Fermi velocity component  $v_x$ ); rather than using the band dispersion  $E_{\vec{k}}$  in the full energy range, its effective model can often be constructed which is easier to handle and offers better insight, e.g. into how the magnetisation direction and spin-orbit interaction influence the band anisotropy<sup>51</sup>. At this point, we remark that through such anisotropy, the plasma frequency (12) may become anisotropic: in a non-magnetic cubic crystal, for

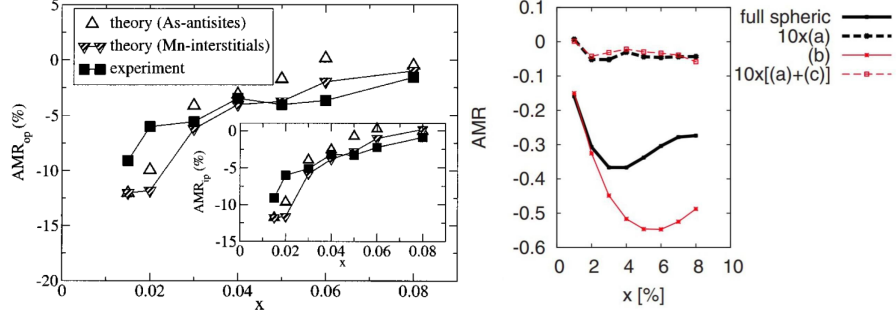


FIG. 5: *Left*: Measured AMR in the dilute magnetic semiconductor (Ga,Mn)As with doping  $x$  varied<sup>58</sup>. *Right*: Modelling allows to distinguish the intrinsic (a) and extrinsic (b,c) mechanisms of AMR; clearly, the extrinsic mechanism (b) as defined in Ref.<sup>17</sup> dominates. Reproduced from (left) Ref.<sup>58</sup> and (right) Ref.<sup>17</sup>.

example,  $\omega_{p;xx} = \omega_{p;yy}$  but when magnetic order is present,  $\vec{m} \parallel \hat{x}$  breaks this symmetry. For the definition of such anisotropic  $\omega_p$  and its discussion related to intrinsic AMR, see Ref.<sup>12</sup>.

Turning our attention to the scattering, we first remark that should the resistances in Eq. 1 be calculated as  $\propto 1/\sigma_0$  of (3) for different directions of  $\vec{m}$ , whereas  $\tau$  remains constant, the result is independent of  $\tau$ . In other words, while scattering had to be taken into account to obtain finite conductivity  $\sigma_0$ , it has no influence on the AMR. This is, however, only the simplest situation possible: in most cases,  $\tau$  does indeed depend on the direction of  $\vec{m}$  and this can either become manifest in the matrix elements  $M_{kk'}$  of the scattering operator (below, we give an explicit example) or the direction cosine in Eq. 13. The latter opens a pathway for the current direction to enter directly the calculation of scattering time:  $\tau$  in the relaxation time approximation<sup>52</sup> depends on  $\vec{k}$  and the Boltzmann expression for conductivity<sup>53</sup> assigns the largest weight to  $\tau(\vec{k})$  with  $\vec{k}$  parallel to the current direction.

Such was the approach to understanding the AMR in elemental ferromagnets (notably, nickel or iron) since the seminal work of Smit<sup>54</sup>. The ratio  $\alpha$  of resistivities in majority and minority spin channels (within what was later<sup>55</sup> called the *Smit mechanism*) allows to express the difference  $\Delta\rho = \rho_{\parallel} - \rho_{\perp}$  with respect to the direction of  $\vec{m}$  as

$$\frac{\Delta\rho}{\rho} = \gamma(\alpha - 1) \quad (14)$$

where  $\gamma \approx 10^{-2}$  describes the competition of spin-orbit interaction and exchange interaction. For these simple cases it holds that  $\alpha > 1$  (thus  $\rho_{\downarrow}(T=0) > \rho_{\uparrow}(T=0)$ ), so that the AMR is always positive and the other cases are described in Fig. 2. It should be stressed that

formula 14 provides only a basic guidance to AMR, yet it is referenced occasionally up to nowadays<sup>56</sup> when interpreting experiments; we return to the discussion of *sd* models applied to AMR in elemental metals and their alloys in Sec. 3III A and proceed now to discuss the effective models in dilute magnetic semiconductors (DMS).

While the previously discussed *sd* models<sup>1</sup> treat the band structure only on a rudimentary level, essentially  $\omega_p$  in (3) is taken as coming from a single band and independent of  $\vec{m}$ , models of transport in DMS are more elaborate in this respect. The valence band  $E_{\vec{k}}$  can be obtained<sup>57</sup> from four- or six-band models (depending on the needed level of detail) and conductivity can be evaluated using the Boltzmann equation, see Sec. 3III B. It turns out<sup>17</sup> that the relaxation time approximation (RTA) with a constant (magnetisation-direction independent)  $\tau$  leads to a too small AMR so that in the particular case of (Ga,Mn)As, extrinsic mechanism (i.e. anisotropy of  $\tau$ ) is dominant. The main source of scattering, magnetic atoms (manganese) substituting for cations of the host GaAs lattice, features magnetic and non-magnetic part (their ratio is described by parameter  $\alpha_{sc}$ ) and while analytical estimates using Eq. (13) such as

$$\text{AMR} = -\frac{20\alpha_{sc}^2 - 1}{24\alpha_{sc}^4 - 2\alpha_{sc}^2 + 1}$$

can be obtained under simplifying assumptions, the full model shown in Fig. 5 reproduces the measured<sup>58</sup> AMR well. Also, various combinations of scattering and SO effects in two-dimensional electron gases have been explored: extrinsic anisotropy in Dirac fermions<sup>59</sup> or Rashba system<sup>51,60,61</sup>.

Turning our attention back to transition metals (see Tab. II in<sup>1</sup> for a list of material systems), two important publications should be mentioned. Mott<sup>62</sup> proposed that resistance in metals at high temperatures mainly depends on the scattering of 4s electrons into 3d states. At low temperature, the d-states are mainly populated, so that the main scattering is due to s-s-scattering and the resistivity is significantly lower. Smit applied this idea first to AMR<sup>54</sup> and proposed that the AMR can be only due to spin-orbit interaction (i.e. neglecting the possibility of intrinsic AMR), should always be positive and explained the larger AMR measured in dilute alloys by scattering due to foreign ferromagnetic atoms, where in simple transition metals (e.g. Ni) it is due to non-magnetic ions, lattice vibration or irregular stress. The foreign ferromagnetic atoms are supposed to have a larger effect on AMR than the other scattering effects, which also causes the AMR to decrease with increasing temperature (since lattice vibrations are becoming a more dominant contribution

in resistance at higher temperatures)<sup>54</sup>.

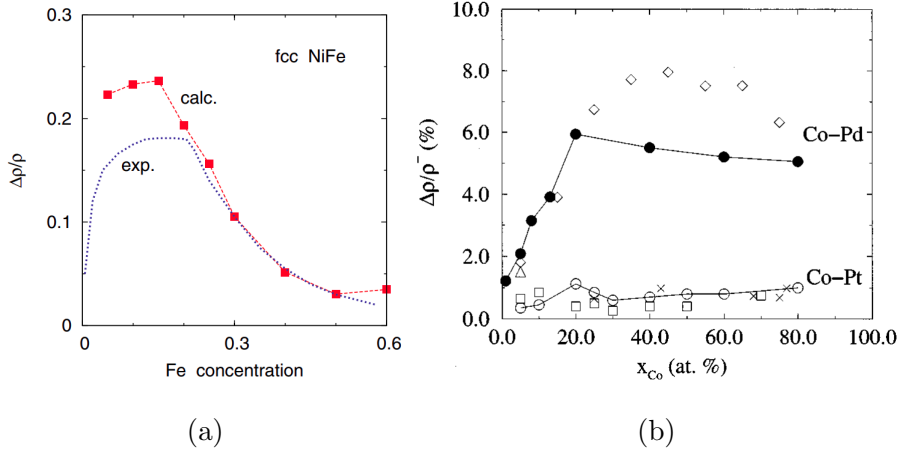


FIG. 6: AMR in alloys (a) nickel-iron, (b) cobalt with non-mag. elements. Reproduced from (a) Ref.<sup>65</sup> and (b) Ref.<sup>28</sup>.

## 2. *Ab initio* models

Most materials lack the simplicity of electronic structure which would render construction of its effective model practicable. Band structure can nevertheless be obtained by ab initio methods (DFT or beyond) and should the AMR be dominated by intrinsic mechanism, plasma frequency for different magnetisation directions can be calculated. Alternatively, conductivity can be obtained using Green's functions  $G = G^+(E_F)$  in Kubo formula<sup>63</sup>

$$\sigma_{\mu\nu}(E) = \frac{e^2\hbar}{\pi V} \text{Tr} \langle v_\mu \text{Im} G v_\nu \text{Im} G \rangle \quad (15)$$

by replacing the disorder average with  $\tilde{G}v_\nu\tilde{G}v_\mu$  and  $\tilde{G}^{-1} = E - H - i\Gamma$  with constant  $\Gamma$  (which in the limit  $\Gamma \rightarrow 0$  drops out from the expression for AMR). When extrinsic mechanisms of AMR are important a better treatment of scattering is needed and selfenergy  $\Sigma$  (whereas  $\text{Im} \Sigma = \Gamma$ ) must also be calculated by ab initio techniques.

The first attempt at such calculation has been undertaken by Banhart and Ebert<sup>63</sup> who employed the coherent potential approximation (CPA) but AMR as a function of  $x$  (Fig. 1 in that work) was overestimated. Further refinements were made<sup>64</sup> and more recent calculations of  $\text{Fe}_x\text{Ni}_{1-x}$  achieve a nearly quantitative agreement<sup>65</sup> to experimental AMR values. A different approach, based on modelling the system by layers also reproduces well<sup>66</sup> the experimental data on permalloy or Fe-Co<sup>67</sup> systems. Temperature-dependent AMR has now

also been studied<sup>68</sup>. Beyond this material, cobalt alloys (with Pt or Pd<sup>28</sup>) and nickel alloyed with Cu or Cr<sup>69</sup> were studied, to give two examples among many. AMR in permalloy doped by selected transition metals (see Fig. 2 in Ref.<sup>68</sup>) agrees reasonably well with ab initio calculations with the exception of doping by gold but it is presently unclear whether this is a failure of CPA (in this particular case) or an experimental issue<sup>70</sup>. Recently, it has been argued (based on the same theoretical technique) that in iron cobalt<sup>11</sup> the AMR is driven by intrinsic mechanism.

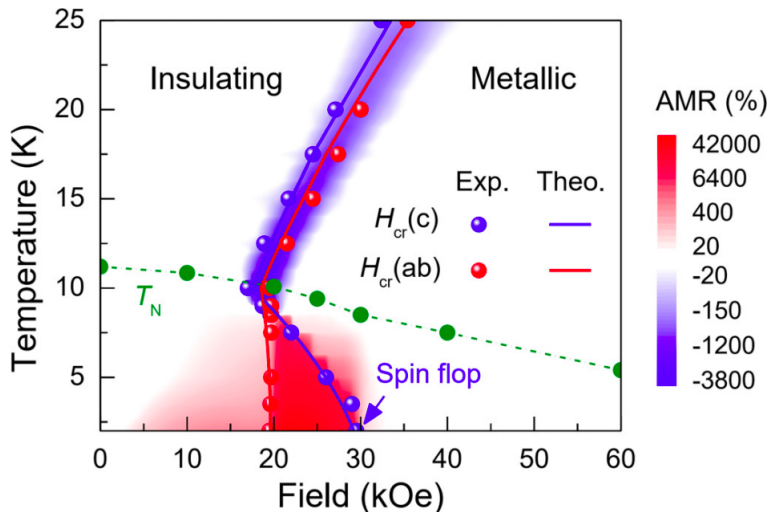


FIG. 7: Magnitude of AMR in antiferromagnetic  $\text{EuTe}_2$  where band structure changes from insulator to semi-metal depending on the configuration of magnetic moments (which can be manipulated by applied magnetic field). Reproduced from Ref.<sup>73</sup>.

### C. Further remarks

We conclude this section by several theoretical remarks before we proceed to discussion of AMR in particular materials.

*Hexagonal systems.* In cubic systems, resistivity tensor reduces to a number  $\rho_0$  (i.e. it is proportional to identity matrix); we will now show that the same is true also for hexagonal systems. Assume that  $\hat{x}$  is parallel to one of the sides of the hexagon. The two components of the resistivity tensor are denoted as  $\rho_{\parallel}$  and  $\rho_{\perp}$  again. Then, if the tensor is rotated by an angle  $\theta$ , its new form equals the form presented in Eq. 5. In a hexagonal system, a rotation of  $\theta = \pi/3$  is a symmetry operation and must not alter its properties. In this case, the zero

off-diagonal elements must be conserved. In order to fulfill the equation  $0 = \frac{1}{2}\Delta\rho \sin(\frac{2\pi}{3})$ , we have to demand  $\Delta\rho = \rho_{\parallel} - \rho_{\perp} = 0$ . Plugging this into Eq. 5, the resulting resistivity tensor  $\rho = \rho_0 \cdot \mathbf{I}_2$

*Metal-to-insulator transition.* A very large change of electric conductivity can be achieved by tuning the system between metallic and insulating regimes: typical system being vanadium dioxide<sup>71</sup>. While such typical MIT behaviour is unrelated to magnetism, proposals of magnetic-order-dependent gap opening have appeared for orthorhombic CuMnAs<sup>72</sup> and experimentally, semimetallic antiferromagnet EuTe<sub>2</sub> discussed in Sec. 3(c) is the first system where the transition between low- and high-resistance states was achieved<sup>73</sup> by rotating the magnetic moments as the phase diagram in Fig. 7 shows. This effect can be understood as the extreme case of intrinsic AMR: rather than deforming Fermi surface (FS) slightly by rotating the magnetic moments, the FS disappears altogether. A related effect can also occur in magnetic topological insulators, see Sec.4b IV B 4.

*Relative and absolute AMR.* It is customary to evaluate the AMR in relative terms. This makes good sense for extrinsic AMR where both  $\rho_0$  and  $\Delta\rho_0$  are proportional to the density of scatterers  $n_{imp}$  and the ratio (1) is then independent of  $n_{imp}$ . Fig. 4 in<sup>2</sup> demonstrates that this may be true for a large group of samples. On the other hand, when resistivity comprises two additive parts (in the spirit of Matthiessen's rule) where one is anisotropic and the other is not, it is more meaningful to focus on absolute difference of resistivities for magnetic moments parallel and perpendicular to current. This is also the case for polycrystalline samples where the isotropic part of resistivity is due to scattering on grain boundaries: a suitable approach is then the Fuchs-Sondheimer theory discussed e.g. in the introduction of Ref.<sup>74</sup>.

### III. MATERIALS

#### A. Elemental ferromagnets (TMs) and their alloys

First observation of AMR was made in iron and nickel with cobalt following (see Sec. II B for the history) and understandably, the first microscopic theories therefore aimed at ele-

mental ferromagnets. The first step beyond the quantification of the AMR ratio on the level of Eq. 1 was to analyse individual symmetry contributions to the AMR<sup>5</sup> (as given by Eq. 11 or Eq. 10 nowadays) and next, their temperature dependence was determined<sup>75,76</sup>. Other papers on these materials are discussed in Sec. 2(b)II B 2 since the results of them are outdated by now, but of great historical importance in the development of models. In the following, the most interesting results are discussed and at the end of this section, typical AMR values are listed in table I. There is some scatter in the values of AMR, whose origin cannot be conclusively identified, since part of the information is lacking in some of the studies. So it is unclear whether in all studies the saturation magnetization is reached, what is the crystal structure and crystalline quality and in very thin films, surface scattering can even play a role. Important observables to watch are the sign of the AMR and the order of magnitude of the values.

State-of-the-art reports of AMR in the three transition metals are for iron thin layers by van Gorkom et al.<sup>75</sup> and for nickel films by Xiao et al.<sup>77</sup>. While these two metals are cubic, the situation is somewhat more complex for cobalt which exists in the hcp<sup>78</sup> and fcc<sup>79</sup> phases. In polycrystalline samples<sup>33</sup>, the AMR is a factor of about 1.8 larger for fcc than for hcp (hexagonal close packing). This behavior was explained by differences in (calculated) DOS at the Fermi level. The hcp-Co AMR is reported to lie between 1.14 and 1.23 % and for predominantly fcc-Co samples the span is 1.73 to 2.19%.

Polycrystalline Co has a dominant intrinsic AMR contribution, which was shown by frequency-dependent studies<sup>12</sup> on ac-AMR (See Sec. 4IV B for details on the ac-AMR method). In the same study, it was also shown experimentally that polycrystalline Ni and the alloys  $\text{Ni}_x\text{Fe}_{(100-x)}$  with  $x = 50$  and  $x = 81$  (permalloy) have a negligible intrinsic contribution and plasma frequency calculations indicate a similar behavior in single-crystalline materials. For the single-crystalline case an experimental confirmation is still required. For iron, such investigations are lacking entirely and it is thus unknown whether the AMR in Fe is caused by extrinsic or intrinsic contributions.

In the analysis of Döring<sup>5</sup> based on Eq. 11 or Eq. 10, four-fold signals were also identified in single-crystalline nickel. However the reporting of higher-order signals in these basic TMs is rare<sup>77</sup> and usually only two-fold signals are reported. In some studies, deviations from two-fold AMR are accounted for by magnetocrystalline anisotropy using Stoner-Wohlfarth approaches as for example was reported by Miao et al. in single-crystalline Co and poly-

crystalline  $\text{Fe}_{20}\text{Ni}_{80}$ <sup>80</sup> as well as in epitaxial  $\text{Fe}_{30}\text{Co}_{70}$  thin-films<sup>21</sup>.

Alloys offer a vast field for research on AMR, since the effect can be increased significantly, as compared to the pure TMs, by tuning their composition. Our discussion of alloys is split into two categories: first, the three basic TMs with small amounts of TM impurities are discussed and second, we focus on alloys made from a combination of the three basic TMs. The best known example of the second category is Permalloy ( $\text{Ni}_{80}\text{Fe}_{20}$ ). Typical values of AMR ratios are listed for the alloys in table I as well.

A comprehensive work on the first category of alloys, nickel with TM impurities, is Jaoul *et al.*<sup>55</sup>. An important characteristics of these impurities is the virtual bound state (VBS); when the VBS appears<sup>81</sup> (for example with V, Cr, Os or Ir) both positive and negative AMR was measured and otherwise the AMR remains positive (this was the case with Mn, Fe, Co, Pd, Cu, Zn, Al, Si, Sn and Au where the VBS does not appear). This was attributed to the effect of the  $L_z S_z$  operator of the spin-orbit interaction on the VBS, which was included into the description of AMR by adding the term  $+3\beta\alpha/(\alpha + 1)$  to formula 14, where  $\beta$  encrypts the effect of the  $L_z S_z$  term. It can be positive or negative, thus the AMR can show both signs. Please note, that this explanation for negative AMR is consistent with the more recent and elaborate one given by Kokado and Tsunoda<sup>15</sup> (see sec. IB). In contrary to the latter ones, the extension of Eq. 14 by Jaoul is limited to strong ferromagnets and is not capable of describing e.g. features of half-metals such as spin-dependent effective mass. In another study by McGuire *et al.*<sup>82</sup>, robust negative AMR up to room temperature (RT) was achieved by considering Ir as an impurity in various hosts such as nickel, cobalt, iron and in certain alloys of these three.

In the second category of alloys we find the combinations FeCo, CoNi and NiFe as well as FeCoNi in diverse compositions. AMR in these alloys is robust and typically one order of magnitude larger than in the pure TM as can be seen in table I. Many publications focus on AMR measurements for different compositions and track the dependency of AMR on concentration of a certain element. Of special interest is permalloy, which shows not only a large AMR, but is also used in a number of industrial applications, for example in magnetic readout heads. The interest of industry is due to its nearly zero magnetostriction and high magnetic permeability.

Composition-dependent studies of the AMR ratio in the nickel-based alloys  $\text{Fe}_x\text{Ni}_{1-x}$ ,  $\text{Co}_x\text{Ni}_{1-x}$  and  $(\text{Co}_x\text{Ni}_{1-x})_{86}\text{Fe}_{14}$  are provided by Ishio *et al.*<sup>83</sup> and in the iron-based alloys

NiFe and FeCo by Berger *et al.*<sup>84</sup>. In the first case of the nickel-based alloys Ishio *et al.* investigated the AMR ratio for two different current directions [001] (which they call  $K_1$ ) and [111] (which they call  $K_2$ ). Extremal values of AMR are achieved for  $(\text{Ni}_{80}\text{Co}_{20})_{86}\text{Fe}_{14}$  with  $K_1 = +68\%$  and  $K_2 = -32\%$ . For  $K_2$  there is an increase leading to a sign change to positive values with increasing Fe and Co<sup>83</sup>. This is consistent with other measurements reporting AMR of up to 50% in NiCoFe alloys with a maximum at  $\text{Ni}_{80}\text{Co}_{20}\text{Fe}_5$ <sup>85</sup>. In the FeNi alloys, a maximum AMR ( $K_1$ ) of ca. 35% is achieved at ca. 10-15 % Fe. Permalloy shows an AMR of 25%<sup>83</sup>. In the second case of the iron-based alloys by Berger *et al.*, the AMR is split into an impurity-based AMR contribution  $(\frac{\Delta\rho}{\rho})_{im}$  and a phonon-based contribution  $(\frac{\Delta\rho}{\rho})_{ph}$ . Both contributions are individually plotted vs. the iron concentration.  $(\frac{\Delta\rho}{\rho})_{ph}$  is positive for the case of weak electron scattering in Fe-Co and negative in the case of strong, resonant electron scattering in the other alloys. The impurity contribution is always positive and larger for the strong scattering. A peak AMR of ca. 16% is found for permalloy. A more recent study<sup>80</sup> reports only few per cent AMR for sputtered  $\text{Ni}_{80}\text{Fe}_{20}$  films but in absolute terms, i.e.  $R_{\parallel} - R_{\perp}$  in Eq. 1, the anisotropy is similar in both samples; here, the buffer layer thickness also plays role<sup>86</sup> most likely through changing the background resistivity. AMR in epitaxial  $\text{Fe}_{30}\text{Co}_{70}$  was shown to have strong crystalline terms<sup>21</sup>. More alloys involving transition metals are discussed in Sec. 3(f).

A comparison of experimental data and CPA calculations is given in Fig. 6(a), where the AMR ratio is calculated for fcc NiFe alloys dependent on the Fe concentration. Especially for concentrations larger than 0.15, the calculations describe the experimental data almost perfectly. Calculations of dilute NiFe thin-film, wires and FM/non-magnetic/FM multilayers using Boltzmann equation with RTA and a two-current model are carried out by Rijks *et al.*<sup>74</sup>.

## B. Dilute Magnetic Semiconductors

A completely different perspective of AMR is offered by the dilute magnetic semiconductors (DMSs): magnetism and transport properties can be tuned in these systems to some extent independently. Our understanding of the electronic structure in DMSs relies on the solid knowledge about III-V (and other) systems such as GaAs combined with substitutional effect of a magnetic element (typically manganese) whereas coupling between localised mag-

Material	AMR percentage	Remarks
Fe	0.2 - 1.5	RT <sup>87</sup> to low temperature (LT) <sup>75</sup>
Ni	1.8 - 3.15	see Tab. I in <sup>2</sup> and also Fig. 1a
Co	0.3 - 3.5	from <sup>33</sup> ; Fig.1 in <sup>13</sup>
Ni with Pd	2	$T = 4.2$ K; impurity without VBS <sup>55</sup>
Ni with Zn	6.5	low temperature; impurity without VBS <sup>55</sup>
Ni with Cr	-0.28	$T = 4.2$ K; impurity with VBS <sup>55</sup>
...		
Co with 3% Ir	-2.56	RT; <sup>82</sup>
...		
Co <sub>45</sub> Pd <sub>55</sub>	7.96	$T = 4$ K; <sup>137</sup>
...		
Ni <sub>80</sub> Fe <sub>20</sub> (permalloy)	16 - 25	LT and RT <sup>84</sup> ; $T = 10$ K <sup>83</sup>
(Ni <sub>80</sub> Co <sub>20</sub> ) <sub>86</sub> Fe <sub>14</sub>	+68 and -32	[001] and [111] current direction, resp. <sup>83</sup>
Ni <sub>77</sub> Fe <sub>22</sub> Cr <sub>2</sub>	0.76	$T = 4.2$ K; <sup>31</sup>
...		

TABLE I: Examples of AMR values for three groups of TM-based systems: pure room temperature (RT)-FM metals (i.e. Fe, Co, Ni); the basic TM with TM-impurity; and alloys of the three basic TM. More examples of Ni-alloys with other TM impurities can be found in table 1 of<sup>55</sup> and more example of alloys with Ir as impurity are listed in table 1 of<sup>82</sup>. AMR for other concentrations of Pd in CoPd are listed in table 1 of<sup>137</sup>, where the given composition Co<sub>45</sub>Pd<sub>55</sub> shows the maximum value. A broader listing of the nickel-based alloys FeNi, CoNi and (CoNi)Fe is found in<sup>83</sup> and of the iron-based alloys NiFe, FeCr, FeV and FeCo in Fig. 1b and Fig. 2 of<sup>84</sup>. AMR values for NiFeCr with higher concentrations of Cr are listed in Tab. 1 of<sup>31</sup>.

netic moments (provided in that case by  $3d^5$  electrons) is mediated by delocalised carriers<sup>57</sup>. The key parameter is the acceptor (in case of III-V:Mn) binding energy  $E_0$  and also its physical origin<sup>88</sup> indirectly influences the magnetotransport mechanism.

Given the appreciable spin-orbit interaction in GaAs ( $\Delta_{SO} = 0.34$  eV) and basically metallic conduction (Fig. 32 in<sup>57</sup>), AMR could have been anticipated to occur in (Ga,Mn)As. Indeed, the first report of AMR in (Ga,Mn)As<sup>89</sup> has soon been followed by more detailed

studies<sup>58,90</sup> and new ideas keep appearing (co-doping by lithium<sup>91</sup> or As/Sb substitution<sup>92,93</sup>). These studies allowed to explore the AMR under continuous variation of band-structure parameters and filling as well as of strain<sup>8,39</sup>.

Research on AMR in DMSs has pushed the understanding from 'complicated to simple' concepts: idealised *sd* models<sup>1</sup> gave way to a semiquantitative description<sup>94</sup> where the intrinsic and extrinsic sources of AMR<sup>12</sup> could be separated (see Sec. I D and then the detailed discussion of microscopic models in Sec. II). An application of this model is shown in Fig. 8, where a Stoner-Wohlfarth model as well as four-fold crystalline AMR terms have to be taken into account. In the lower panel of b) it can be clearly seen that an attempt of fitting the data to terms without four-fold terms leads to insufficient agreement. Currently, interest in the once very popular (Ga,Mn)As subsides since the prospects for the RT magnetism<sup>95</sup> remain unfulfilled. Nevertheless, Mn-doped III-V semiconductors remain a good test-bed for exploring transport phenomena in materials with tunable magnetic properties.

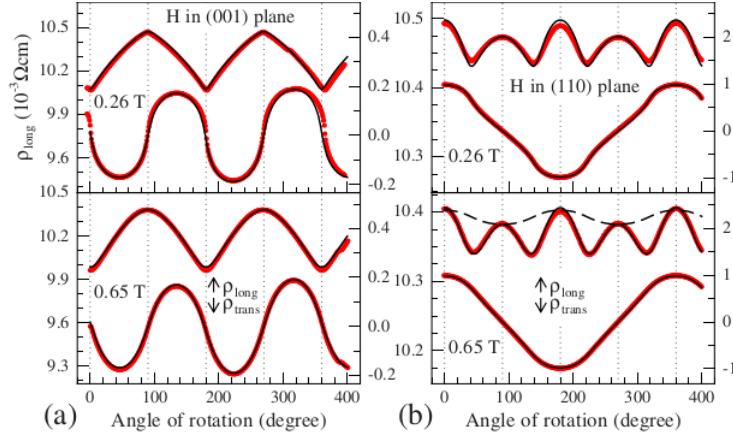


FIG. 8: The data (red thick lines) and fit (black thin line) of the longitudinal resistivity  $\rho_{\text{long}}$  (upper line in every plot) for current direction along [110]. A magnetic field of 0.26 and 0.65 T are rotated in the (001) and (110) plane, respectively. The dashed line in the lower panel of b) refers to an attempt of fitting the data to  $\cos(2\phi)$ , which is clearly insufficient. The lower lines in every plot are the transversal resistivity. Reproduced Detail from Fig. 7 in Ref.<sup>39</sup>.

Despite the versatility of this material class, not much attention was given to other DMS: two-fold and eight-fold AMR were reported in a 10 nm film of (In,Fe)As in<sup>48</sup>. In a 100 nm film of the same material, the eight-fold component was missing, which was attributed to higher electron concentration. Yet this claim is not supported by microscopic calculations

and, together with the very small magnitude of AMR and low electron concentrations, this may well be a hint that it is not the absence of *sd*-scattering at the Fermi surface<sup>48</sup> but issues with sample quality that lead to this unusual behaviour. Better established materials, in terms of sample quality, such as (Cd,Mn)Te still suffer from too low carrier concentration<sup>49</sup> and even if the regime of metallic conduction is reached<sup>96</sup>, only magnetoresistance (rather than its anisotropy) is measured and transport mechanisms seem to be less well-established than in the case of (Ga,Mn)As. These systems also occasionally suffer from the formation of multiple phases<sup>97</sup>. Finally, magnetically doped  $A_2B_3$  systems (where A is either Bi or Sb and B is Se or Te) should be mentioned<sup>98</sup> or<sup>99</sup>. Finally, magnetically doped ZnO should be mentioned<sup>100</sup> whereas the mechanism of magnetic state formation is complicated and the latter can even be achieved by hydrogenation of ZnO<sup>101</sup>.

### C. Antiferromagnets

While ferromagnetism has been a known phenomenon since ancient times, its counterpart antiferromagnetism was introduced no earlier than in 1933 by Landau<sup>102</sup>. It is little surprising then, that AMR in this material class has only recently been investigated. A little less than ten years ago, first studies appeared reporting AMR in antiferromagnetic (AFM)  $Sr_2IrO_4$ <sup>103,104</sup> and in FeRh which undergoes a transition from antiferromagnet to FM<sup>105,106</sup>. In recent years, the class of AFM materials has received more attention due to the development of AFM spintronics<sup>108</sup>. The hope is to revolutionize spintronic applications by making use of advantageous properties of AFMs such as robustness against magnetic field perturbations, the lack of a stray field or ultrafast dynamics. A prototypical magnetic memory was developed using CuMnAs, see Sec. 4(c), and the transversal component of AMR (also called the planar Hall effect), was used as readout<sup>109</sup>. As tetragonal CuMnAs has thus become a popular AFM material<sup>110</sup>, its properties came under intense scrutiny; microscopic mechanism of its AMR is however far from clear<sup>38</sup>: multiple kinds of impurities lead to AMR which is comparable to experiment. On the other hand, intrinsic AMR linked to gap opening controlled by Néel vector orientation was proposed<sup>72</sup> to occur for the orthorhombic phase<sup>111</sup> of CuMnAs which is similar<sup>112</sup> to another AFM metal:  $Mn_2Au$ .

Another material which is a candidate for magnetic memory is MnTe: Next to a robust, continuously varying AMR signal suitable as readout for AFM states, stability of the AFM

states against perturbing magnetic field itself was shown by means of zero-field-AMR (zf-AMR)<sup>36</sup>: resistivity is measured in zero magnetic field at low temperatures after the sample is field-cooled in a *writing field*. After taking a data point, the sample is heated up again and the procedure repeated for another orientation of the writing field. Repeating this for a continuous rotation of writing fields yielding a periodically zf-AMR signal resembling the conventional AMR. Furthermore, in the experiment it was shown that for a writing field of 2 T, the zf-AMR is multistable against perturbations from magnetic fields of 1 T or less. Hence, the possibility of writing and readout combined with robustness against perturbing fields makes it an excellent candidate for a spintronic device<sup>36</sup>. Also, crystalline AMR measured in the Corbino geometry shown in Fig. 9 shows a strong  $\cos 6\varphi$  component due to the hexagonal crystalline structure of MnTe<sup>46</sup>.

Point-contact measurements in single-crystalline bulk sample of the AFM Mott-insulator Sr<sub>2</sub>IrO<sub>4</sub> at liquid nitrogen temperature yielded a field-dependent transition from four-fold AMR (low field) to two-fold AMR (high field). The four-fold AMR was interpreted as crystalline AMR reflecting the tetragonal crystal structure of the single-crystalline sample, while the transition to two-fold AMR being due to canting of AFM moments. The AMR ratio shows a maximum of 14% at a field of 120 mT. The large AMR has been attributed to large SOC in this 5d oxide<sup>104</sup>. In another experiment, AMR in a Sr<sub>2</sub>IrO<sub>4</sub> film is studied by utilizing a SiO/La<sub>2/3</sub>Sr<sub>1/3</sub>MnO<sub>3</sub> (LSMO) heterostructure. The ferromagnetic LSMO is used to control the reorientation of AFM spin-axis via exchange spring effect. The AMR at low temperatures ( $T = 4.2$  K) is showing a 4-fold behavior, while at intermediate temperatures ( $T = 40$  K) no AMR signal was detected and at higher temperatures ( $T = 200$  K) the AMR is dominated by the two-fold AMR of the FM LSMO<sup>103</sup>.

An AFM memory in FeRh was proposed by Marti *et al.* where field-cooling is used to write a magnetic state and AMR used as readout. Similarly to MnTe<sup>36</sup>, the memory shows a certain insensitivity against perturbing fields<sup>105</sup>. RhFe undergoes a FM-AFM transition. It is antiferromagnetic below  $T_N = 370$  K and ferromagnetic between  $T_N$  and  $T_C = 670$  K. Transport was investigated for both phases by means of first-principle calculations (relativistic TB-LMTO). AMR exists in both the FM and the AFM phase and was stated to be in a range of up to 2% depending on the Rh-content. The AMR in the AFM phase is larger for most of the investigated compositions<sup>106</sup>.

A rather special case are single-crystals of AFM EuTe<sub>2</sub> where a peak value of 40000 % at 2

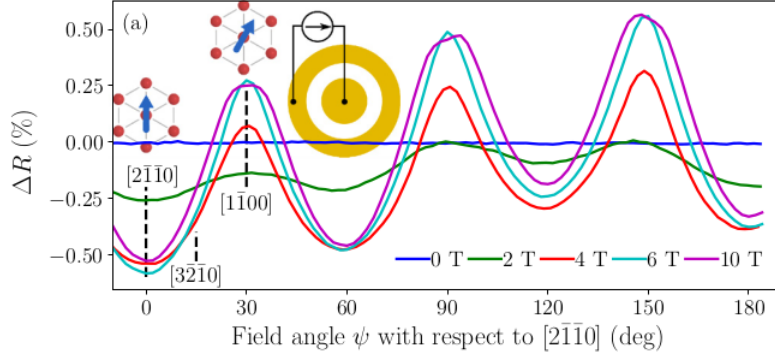


FIG. 9: Crystalline AMR measured in MnTe for different field strengths using a Corbino geometry. The AMR shows a six-fold symmetry, which can be expected for the crystalline AMR in a hexagonal material. Reproduced from Ref.<sup>46</sup>.

K and 22 kOe (2.2 T) is achieved due to a metal-insulator phase transition (MIT). Since the MIT shows different critical fields for the ab-plane and the c-axis, the AMR becomes colossal for applied field values between the in-plane and the out-of-plane critical fields leading to a several order of magnitude change in resistivity for rotating the magnetic field. Bandstructure calculations confirmed this behavior. AMR for fields and temperatures entirely within one phase (metallic or insulating) is in an order of magnitude of less than 20% and thus comparable to other materials<sup>73</sup>. Finally, we remark that (collinear) ferrimagnets can be considered to belong to this group too<sup>107</sup>, since they equivalently have two magnetic sublattices, with the difference that the magnetic moment is not fully compensated. Furthermore, AMR in non-collinear AFMs is a rather novel topic and will be discussed in sec. 4b-IV B 3.

#### D. Heusler alloys

*Introduction.* Heusler compounds exhibit a large variety of fascinating properties, as for example ferromagnetism and antiferromagnetism, thermoelectricity, high spin-polarization, superconductivity and topological features<sup>113</sup>. In general, their formula is  $X_2YZ$ , where X and Y are transition metals and Z is a main group element. X is more electropositive than Y. If X and Y are exchanged, the material is called an inverse-Heusler. There are so-called half-Heuslers, which are given by the formula  $XYZ$ <sup>113</sup>. In general, Heusler compounds have a cubic crystal structure, which can occur in different variations. The first Heusler compound was  $Cu_2MnSn$ , discovered already in 1903, which was a surprise because it was ferromagnetic

while its components are not<sup>114</sup>.

Despite the generality of its definition, a large body of research is focused on cobalt-based Heusler alloys (thus  $\text{Co}_2\text{YZ}$  and Y is typically Mn, Fe or a lighter 3d element), since they generally show important features interesting for potential spintronics applications, such as relatively high Curie temperatures, half-metallicity, large magnetotransport effects and many more.

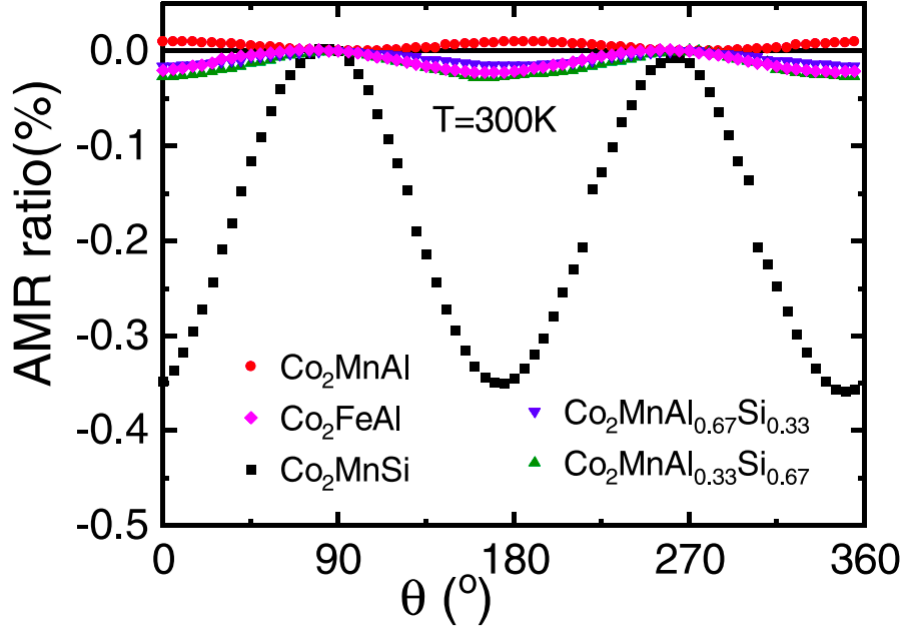


FIG. 10: AMR in  $\text{Co}_2\text{MnAl}$  (CMA),  $\text{Co}_2\text{FeAl}$ ,  $\text{Co}_2\text{MnSi}$  (CMS) and  $\text{Co}_2\text{MnAl}_x\text{Si}_{1-x}$  for  $x = 0.33$  and  $0.67$ . The AMR for CMS has the largest magnitude. All materials exhibit negative AMR except apart from CMA. The order of magnitude of the AMR is in agreement with other studies of Co-based Heusler alloys. Reproduced from Ref.<sup>209</sup>.

*Co-based Heusler compounds.* There is some degree of scatter in the AMR values reported for Co-based Heusler alloys. For example the values for  $\text{Co}_2\text{MnGa}$  were found to lie<sup>20</sup> between  $-2.5\%$  and  $+0.75\%$  depending on current direction and precise stoichiometry. The former dependence can be analysed in terms of crystalline and non-crystalline terms (see discussion later in this Section) as in Fig. 4 but a meaningful comparison between these two, i.e. epitaxial<sup>20</sup> and sputtered<sup>10</sup> samples, requires also the knowledge of background resistivity<sup>19</sup> proportional to  $R_0$  from (1).

On the other hand, once the current direction is fixed (here, along  $[110]$  crystallographic direction) we often arrive at similar characteristics of AMR even for different compounds:

measurements of  $\text{Co}_2\text{MnGa}$  by Ritzinger et al.<sup>10</sup> and of  $\text{Co}_2\text{FeAl}$  by Althammer<sup>7</sup> show negative AMR which decreases with temperature and is quite small ( $\approx 0.1 - 0.2\%$ ). Several other examples are given in Fig. 10.

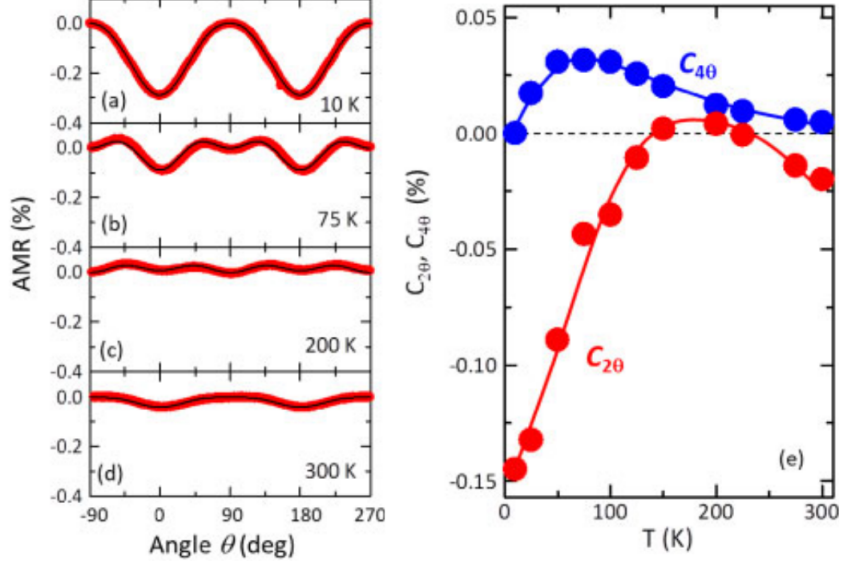


FIG. 11: AMR in  $\text{Co}_2\text{MnSi}$ . (a)-(d) AMR for different temperatures between 10 and 300 K, (e) temperature evolution of the two- and the four-fold Fourier-component of the AMR. Reproduced from Ref.<sup>117</sup>.

Investigation of AMR in  $\text{Co}_2\text{FeZ}$  and  $\text{Co}_2\text{MnZ}$  with  $Z = (\text{Al}, \text{Si}, \text{Ge}, \text{Ga})$  and current along  $[110]$  found both negative and positive AMR, depending on the total number of valence electrons  $N_v$ . If that number was between 28.2 and 30.3, a negative AMR was reported, otherwise a positive. According to bandstructure calculations, in between  $N_v$  of 28.2 and 30.3, it corresponds to half-metallicity<sup>115</sup> as can be seen in Fig. 12. The reported AMR ratios in this paper are relatively small as in the other papers. An equivalent result was achieved in  $\text{Co}_2\text{Fe}_x\text{Mn}_{1-x}\text{Si}$ : Here the AMR is negative for  $x \leq 0.6$  and positive for  $x \geq 0.8$ , which is explained by a transition from minority conduction to majority conduction and thus interpreted as a possible sign for half-metallicity as well<sup>18</sup>. Similarly in  $\text{Co}_2\text{FeSi}$ , the AMR ratio was determined for different samples distinguished by their annealing temperature: Above  $600^\circ\text{C}$  the AMR is negative, up to  $600^\circ\text{C}$  it is positive with the same explanation as before<sup>23</sup>. The AMR ratio in  $\text{Co}_2(\text{Fe-Mn})\text{Si}$ ,  $\text{Co}_2(\text{Fe-Mn})(\text{Al-Si})$  and  $\text{Co}_2(\text{Fe-Mn})\text{Al}$  was reported to be  $\approx -0.2\%$  for low and room temperature<sup>116</sup>.

While the majority of studies focuses on AMR ratio and sign, the symmetry of these

compounds are also a puzzling topic: In  $\text{Co}_2\text{MnGa}^{10}$ ,  $\text{Co}_2\text{FeAl}^7$  and  $\text{Co}_2\text{MnSi}^{117}$ , the AMR showed a complex signal comprising of non-crystalline and crystalline terms. However, the division into non-crystalline and crystalline is usually not made and the AMR is only described in terms of  $\cos(4\phi)$  and  $\cos(2\phi)$  contributions (be  $\phi$  some angle of rotation). The appearing symmetries makes AMR in these materials much more complex as e.g. in simple transition metals, where normally only two-fold symmetries are found. An example of such a rather complex signal in Heusler compounds can be found in Fig. 11.

The 4-fold contributions in these signals are too strong to be ascribed to MCA solely. In a theoretical study by Kokado and Tsunoda<sup>45</sup>, it was suggested that a tetragonal distortion of the crystal structure can introduce such a 4-fold crystalline AMR contribution. Please note, that the Heusler alloys per se have cubic crystal structure, but in thin-films the substrate usually introduces a small tetragonal distortion. Still, despite this explanation being plausible, the complex temperature dependence of the 2- and 4-fold contributions<sup>7,10</sup> asks for further investigation.

In conclusion, a couple of observations can be made for AMR in Co-based Heusler alloys: Firstly, the AMR ratio is generally decreasing for increasing temperature. Secondly, the AMR is very small, often well below 1 % and only in some specific configurations (low temperature, favorable stoichiometry) it reaches up to  $\approx 2\%$ . Thirdly, the AMR ratio given by (1) is usually negative, however can be tuned to be positive. This behavior can be seen consistently in various studies and appears to be a general property of this material class of the Co-based Heusler alloys. Various "phenomenological" explanations for the sign change of AMR are given, e.g. a dependence on annealing temperature, Fe-content, Co-content, current direction and  $N_v$ . These explanations are rather diverging and not allowing for a consistent conclusion. On a microscopic level, however, the various studies can be summarized quite well: as long as the compounds are having a half-metallic character / showing minority conduction, the AMR is negative. In the case of majority conduction and metals not fully polarised on the Fermi level, the AMR becomes positive. It appears to be the case, that the Co-based Heuslers investigated here are all *by default* (= in an ideal configuration) half-metallic, but can be all tuned to lose this half-metallic character (this tuning was done by considering the phenomenological aspects, such as annealing temperature). The theoretical model used to explain it was developed by Kokado and Tsunoda<sup>15</sup>.

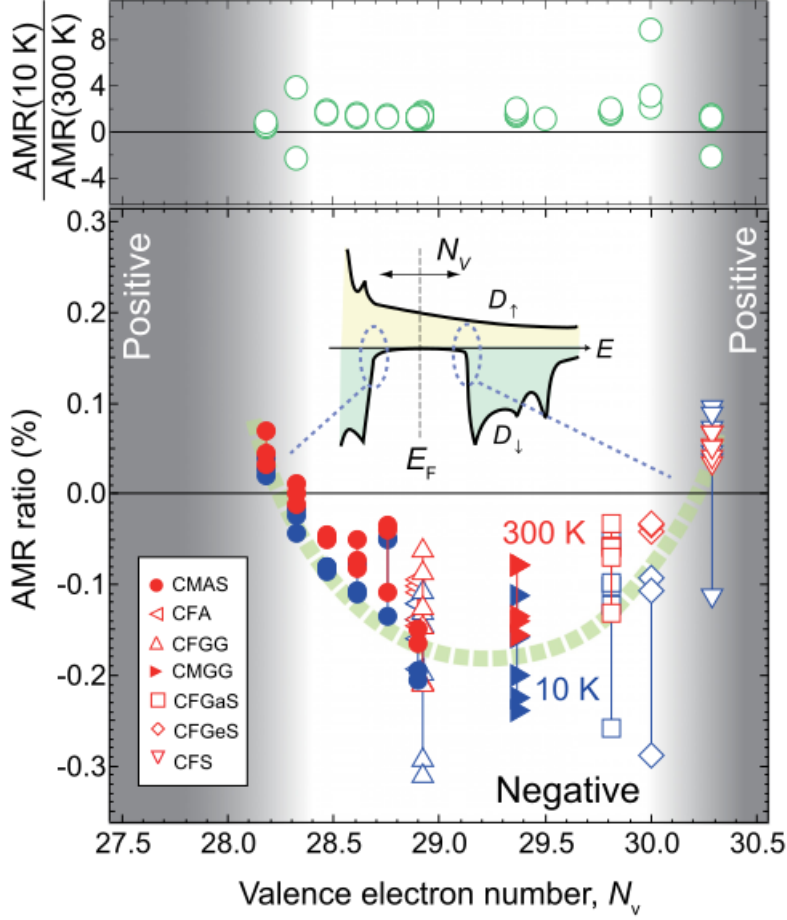


FIG. 12: Valence electron number  $N_V$  dependence of AMR ratio in all  $\text{Co}_2\text{MnZ}$  and  $\text{Co}_2\text{FeZ}$  films. The inset shows the respective density of states. The upper part shows the ratio of AMR ratios at 10 K to 300 K. Reproduced from Ref.<sup>115</sup>.

*Non-Co-based Heusler and semi-Heusler compounds.* Just as with transition metal alloys, Heusler materials<sup>118</sup> span a vast range of compounds: magnetic Heusler alloys include  $\text{NiMnSb}$ <sup>119</sup> or  $\text{Ru}_2\text{Mn}_{1-x}\text{Fe}_x\text{Ge}$ , which is a ferromagnet for  $x = 1$  (no Mn) and an antiferromagnet for  $x = 0$  (no Fe). For  $x = 0.5$  an anisotropy in the MR is observed with a MR of -4% and +2% under parallel and perpendicular configurations of applied field and applied current, respectively. It was speculated, that this (Anisotropic) MR might stem from random alignment of ferromagnetic domains. For  $x = 0$  and  $x = 1$  no MR was found<sup>34</sup>.

## E. Two-dimensional electron gases

*Introduction.* A two-dimensional electron gas (2DEG) can form on various interfaces: surface of liquid helium, classical semiconductor heterostructures or certain transition metal oxide interfaces (TMOI). The textbook example of such a TMOI is a SrTiO<sub>3</sub>/LaAlO<sub>3</sub> (STO/LAO) interface, where the two perovskites individually are non-magnetic insulators<sup>120</sup>. The research interest in TMOIs can be broadly speaking divided into three categories: i) General understanding of the electronic structure, magnetism and related effects, ii) understanding of the superconductivity<sup>121–123</sup> (transition temperature is typically 350 mK<sup>124</sup>) and iii) possible development of applications, such as quantum-matter heterostructures<sup>125</sup>. Regarding AMR in TMOI-hosted 2DEGs, it is important to distinguish whether the transport anisotropy occurs due to orbital effects<sup>126</sup> as discussed in Sec. 1(d) on general level, or if it is indeed related to magnetism. Hysteretic magnetisation loops observed in STO/LAO structures grown at suitable oxygen pressure<sup>127</sup> can be taken as a hint of the latter yet the magnetoresistances shown in Fig. 3 of that reference clearly show that even here, the orbital effects are strong. On the other hand, longitudinal and transversal magnetoresistance (MR) showing similar behaviour of LTO/STO (LTO = LaTiO<sub>3</sub>) at stronger magnetic fields (compare Figs. 2d and e in Ref.<sup>124</sup>) can be taken as an argument that the latter are *not* dominant. The focus of many publications lies on LAO/STO interfaces, whose results are discussed in the following. A summary of AMR in other TMOI-hosted 2DEGs (including LTO/STO<sup>124</sup>) can be found at the end of this section.

*AMR in LAO/STO.* On qualitative level, the AMR of a 2DEG at the LAO/STO interface can exhibit two types of behaviour, see Fig. 13. This was attributed to a phase transition when going to low temperatures  $T$  and high carrier densities  $n$ . A positive and two-fold AMR was found for temperatures  $T > 35$  K, while for lower  $T$  and higher  $n$  negative and showing higher orders up to 6-fold symmetry in (111) and (110) interfaces<sup>121,128–130</sup> was found.

The absolute value of the AMR ratio is not the major point of discussion and should be taken with maximum caution, due to its huge dependence on temperature<sup>131</sup>, current density (AMR increasing with increasing  $n$ <sup>128</sup>),  $B$ -field strength<sup>130,131</sup> and many open points in the understanding of the inner workings of AMR in these materials. The AMR was reported to be larger in the low- $T$  high- $n$  phase ( $\approx 2\%$  below and  $\approx 10\%$  above the critical  $n$ )<sup>129</sup>. A

large value of 110 % was reported for some  $[1\bar{1}0]$  oriented samples grown under low oxygen pressure with  $B = 9 \text{ T}$ <sup>131</sup>, which was understood in terms of oxygen vacancies leading to stronger orbital polarizations and producing a more anisotropic Fermi surface (FS) which leads to larger AMR<sup>131</sup>. Also, the band structure and thus the FS and the AMR are strongly dependent on the sample orientation<sup>131</sup> and oxygen pressure during growth.

In calculations, the AMR is frequently linked to a strong anisotropy of the FSs as exemplified in Fig. 14<sup>126,129,131,132</sup>. Although this means that the AMR is intrinsic, the distinction between intrinsic and extrinsic AMR in these studies is usually not made. The harmonics of the AMR, i.e. the strength of the 2-, 4- and 6-fold are not directly linked to the symmetry of the FS<sup>132</sup>.

The electronic structure at the FS is different between the low- $n$  and high- $n$  regimes<sup>126,132</sup> and is also sensitive to the crystallographic direction of interface<sup>130,132</sup>. The anisotropy appears to be driven by interband scattering, which is suppressed in the low- $n$  regime<sup>132</sup>. The  $t_{2g}$ -orbitals and broken inversion symmetry are generally a central part in the modelling of LAO/STO interfaces<sup>126,129–132</sup>.

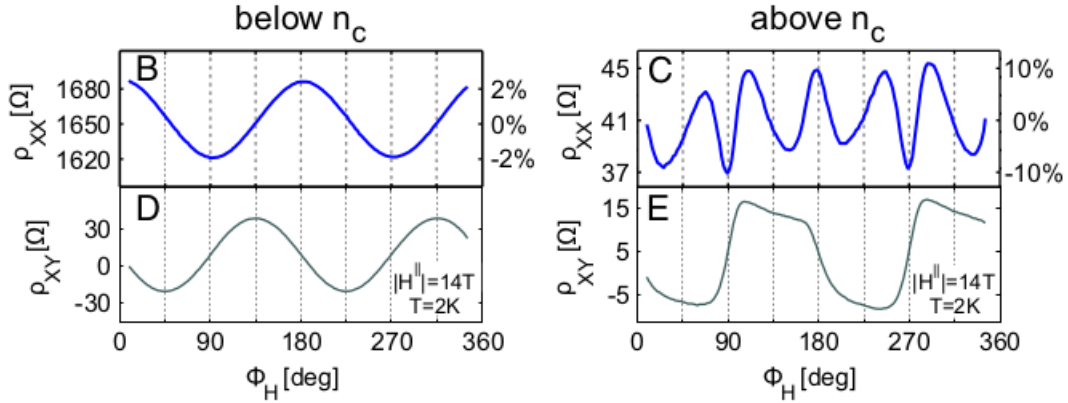


FIG. 13: (B,D) AMR in a 2DEG on LAO/STO interface for electron density below (B) and above (D) the critical value. Reproduced from Ref.<sup>129</sup>.

*Other Materials.* Apart from the much investigated LAO/STO interface, 2DEGs at a TMOI can be found in other material combinations, for example LVO/KVO ( $\text{LaVO}_3/\text{KTaO}_3$ )<sup>133</sup>, LVO/STO<sup>134</sup>, LTO/STO<sup>124</sup> and CZO/STO<sup>135</sup> interfaces where CZO stands for  $\text{CaZrO}_3$  (the last mentioned system stands out by being non-polar without strain). AMR was only studied in the first two examples; sometimes, anisotropic data is shown<sup>124</sup> (longitudinal and transversal MR as mentioned above), although not being referred to as

AMR in the respective publication. The results are shortly summarized in the following. Please note that the similarity of the 2DEGs in LTO/STO and CZO/STO do still suggest the existence of similar AMR phenomena, which yet have to be investigated.

In low temperature measurements in (001)-interfaces of LVO/KVO<sup>133</sup> and LVO/STO<sup>134</sup> a low-field two-fold AMR turned into a high-field four-fold AMR. In case of a (111)-interface of LVO/STO the high-field AMR was six-fold. AMR in LVO/STO showed a strong field- and temperature-dependence. The larger four-fold AMR persisted up to 150 K while the six-fold AMR persisted up to 20 K, similar to the situation in LAO/STO<sup>134</sup>. While no profound explanation was given for the LVO/KVO interface<sup>133</sup>, it was suggested that AMR in LVO/KVO is due to an anisotropic FS, similar to the situation in LAO/STO<sup>134</sup>.

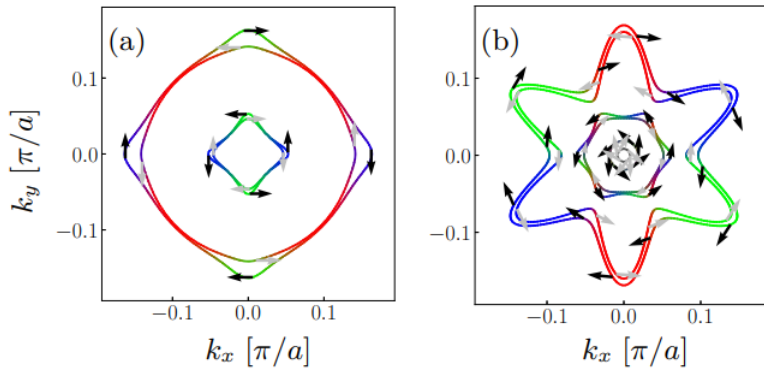


FIG. 14: Fermi surfaces for low-(electron) density spin-orbit coupled 2DEGs at zero magnetic field, with colors indicating orbital content (yz-blue, zx-green, xy-red), and Rashba spin texture indicated by black/gray arrows for opposite chiralities. (a) (001) 2DEG and (b) (111) 2DEG. Both Fermi surfaces are highly anisotropic. Reproduced from Ref.<sup>132</sup>

## F. ...and all the rest

The previous five sections of this chapter were devoted to the material classes showing the most important and remarkable results in the field of AMR. This not nearly a complete picture of the universe of AMR. In the following section we are going to discuss briefly results in several other material classes.

*Fe-based alloys:* Apart from iron-cobalt and iron-nickel alloys which were discussed al-

ready in Sec. 3(a), Berger et al.<sup>84</sup> investigated AMR also in Fe-Cr and Fe-V and split the AMR contributions into parts due to phonon and impurity scattering (see also discussion of Ref.<sup>84</sup> below in the context of CoPd alloy). It was suggested that in alloys with strong scattering the AMR changes sign when the impurity scattering is maximal. According to this study, a change of 3d-DOS does not account for all of the observed behavior.

In  $\text{Fe}_{0.8}\text{Ga}_{0.2}$  it was found that the AMR is two-fold and for in-plane (out-of-plane) configuration at a magnetic field of 500 mT (8 T) showed negative (positive) AMR. Interestingly, with increasing temperature the AMR is constant (decreasing). The AMR ratio is slightly larger than 0.1 % (between ca. 0.2 and 0.5 %). The perfect two-fold shaped AMR curves were interpreted as a sign that saturation magnetization was reached<sup>136</sup>. Properties of NiFeCr alloys such as AMR ratio, low-temperature resistivity and  $T_C$  depending on the Cr concentration are listed in Table 1 of Ref.<sup>31</sup>. A maximum AMR of 0.76% is found in the sample with the lowest Cr concentration of 2%. Increasing the Chromium content leads to a rapid decrease of AMR ratios until the AMR almost vanishes for concentrations higher than 18%. Please note, that this study is using the term *ferromagnetic anisotropy of resistivity (FAR)* instead of AMR. The rapid decrease of the AMR ratio is accompanied by a drop of  $T_C$ , from 778 K for 2% concentration to 48 K at 21% concentration<sup>31</sup>.

*Other alloys or structures involving transition metals.* The AMR of Co-Pd alloys was investigated in Ref.<sup>137</sup> for various cobalt concentrations  $x$  and its temperature dependence was analysed in terms of Parker plots (as discussed in the introduction of Ref.<sup>84</sup>). A maximum ratio of almost 8% was reported at low temperatures for almost equal concentrations of Co and Pd. The results were interpreted with the framework of s-s- and s-d-scattering, splitting the resistivity into contributions of spin up- and down, s-s and s-d-scattering and phonon- and impurity-contribution to the AMR<sup>137</sup>. It can be seen as an advancement of the theory of Campbell, Fert and Jaoul discussed in Sec. 2III A.

Calculated values of the AMR ratio and the residual resistivity of Co-Pd and Co-Pt alloys as a function of the Cobalt-concentration is shown in Figs. 5 and 3, respectively, of Ref.<sup>28</sup>. The values are compared to experimental values from various studies, which showed the accuracy of the calculation. In case of Co-Pt the AMR reaches values of up to 1%, while in the Co-Pd case the AMR shows a maximum of 6% (calculation) or 8% (experiment). The AMR is starkly decreasing for very low Co-content<sup>28</sup>. Note that even for concentrations as low

as 3% of cobalt, palladium alloys remain ferromagnetic<sup>29</sup> and the AMR can be reasonably modelled assuming  $|J| = 43$  meV for the coupling between magnetic moments and highly conductive *s*-electrons.

The in-plane and out-of-plane AMR of Nickel sandwiched by Platinum was experimentally investigated and the symmetry of the AMR discussed<sup>138</sup>. The nickel films are fcc textures with a (111) surface and have a thickness between 2 and 50 nm, while the Platinum layers 5 and 3 nm thick. The in-plane AMR shows only two-fold symmetry as expected for an isotropic polycrystalline sample. The out-of-plane AMR shows pronounced four-fold and six-fold-symmetries for nickel thickness  $\geq 6$  nm. The h.o. symmetries were explained using phenomenological symmetry-based arguments<sup>5</sup> due to (111) textured interface and Fuchs-Sondheimer theory for scattering at interfaces. All results were obtained at room temperature<sup>138</sup>.

The symmetry of Fe-monolayers on a GaAs interface changed depending on the number of monolayers. While for 8 monolayers, a four-fold component was dominant, with decreasing number of monolayers to 6 and 4 the four-fold component decreased. This was attributed to a change of symmetry due to transitioning from bulk-like to interface-like symmetry<sup>139</sup>.

*The perovskite Iron Nitride Fe<sub>4</sub>N and the derived materials CuFe<sub>3</sub>N<sup>140</sup> and Mn<sub>4</sub>N<sup>22</sup>.* For the iron nitride case, we can distinguish into in-plane AMR<sup>107,141,142</sup> and *transverse AMR* (Magnetic field  $\vec{H}$  rotated in the plane perpendicular to the current  $\vec{j}$ )<sup>24</sup>. FeN<sub>4</sub> in the matrix of Fe-doped GaN also exhibits AMR<sup>97</sup>.

In all samples a four-fold component of the AMR was found, for example in in-plane Fe<sub>4</sub>N below 30 K<sup>107</sup>, and it is almost vanishing at higher temperatures. In *transverse* AMR of Fe<sub>4</sub>N and in Mn<sub>4</sub>N the four-fold-component is dominant for low temperatures.

All samples show negative AMR at low temperatures. The AMR in Fe<sub>4</sub>N (in-plane) and in CuFe<sub>3</sub>N remain negative, while Fe<sub>4</sub>N (*transverse*) and Mn<sub>4</sub>N showing positive AMR for temperatures above approx. 50 and 100 K, respectively. Low temperature AMR ratios for Fe<sub>4</sub>N and Mn<sub>4</sub>N scatter between approximately  $-0.75\%$ <sup>107</sup> and  $-7\%$ <sup>142</sup> in iron nitride and around 2 % in manganese nitride<sup>22</sup>). While AMR ratios scatter in general, an increasing AMR ratio for increasing annealing temperature was reported in iron nitride<sup>107</sup>. In the ferromagnetic anti-perovskite  $\gamma'$ -CuFe<sub>3</sub>N, low temperature values in the range of  $-0.067$  to  $-0.336\%$  were reported, at higher temperatures dropping to 0.003%.

In iron and manganese nitride the decrease of the AMR coefficients with increasing temperature show a kink at about 50 K, changing from rapid to moderate decrease. No explanation was given.

The results were discussed in the framework of sd-models<sup>15</sup>. Negative (positive) AMR ratios were linked to minority (majority) spin conduction, while appearing four-fold-symmetries were linked to possible tetragonal distortion. In Fe<sub>4</sub> this was suggested to be due to anisotropic thermal compression<sup>24</sup>.

*Some more perovskites.* Metallic SrRuO<sub>3</sub> exhibits negative magnetoresistance<sup>30</sup> as expected for ferromagnets, and its form for parallel and perpendicular configuration of magnetisation and current confirms this is AMR rather than an orbital effect<sup>143</sup>, the former being negative and achieving quite large values of  $\approx 25\%$  at low temperatures. The AMR is decreasing slowly for low temperature and steeply for higher temperatures above  $\approx 100$  K as it is approaching and surpassing the Curie temperature of  $\approx 140$  K and it does not show any enhancement in the vicinity of the Curie temperature, which is contrary to the results in manganites and was attributed to a missing of the Jahn-Teller effect<sup>144</sup>. The magnetoresistance depends sensitively on strain, however<sup>145</sup>. AMR and PHE were compared at low temperatures and it was found that the AMR is almost double as large as the PHE with  $\approx 14\%$  and  $\approx 7\%$ , respectively<sup>146</sup>, implying sizable crystalline AMR terms. The nonmagnetic SrIrO<sub>3</sub> (SIO) shows AMR for temperatures below 20 K which was interpreted as a sign of a possible ferromagnetic ordering emerging at low temperatures induced by local structure distortion due to lattice strain. The presented data was close to a two-fold AMR. More precisely, the fitting process yielded  $\text{AMR} \propto \cos(1.75\phi)$ <sup>147</sup>. Interestingly, bulk SrIO<sub>3</sub> does not show such behavior and the here investigated film is a thin-film on a SrTiO<sub>3</sub> substrate<sup>147</sup>. In the previous section, we discussed various examples of thin-films on STO substrats forming a 2DEG at about the same temperature accounting for the transport effects. In our judgement, this could possibly account for the emergent AMR at low temperatures.

*Manganites* form a large class of perovskite materials ranging from (the more common) antiferromagnets (such as CaMnO<sub>3</sub><sup>148</sup>) to ferromagnets (less common in ternary<sup>149</sup> and well-established in numerous quaternary systems described below). Often<sup>144</sup>, this material

class is defined as compounds of the form  $X_aY_b\text{MnO}_3$ , where X and Y are a trivalent and divalent cation, respectively, with their respective concentrations  $a$  and  $b$ . The main part of manganites discussed here are based on Lanthanum, for which the second element Y is either Ca<sup>9,150-154</sup>, Pr<sup>32,155</sup>, Sr<sup>157</sup> or Ag<sup>158</sup>). Among the other materials are Nd<sub>0.51</sub>Sr<sub>0.49</sub>MnO<sub>3</sub><sup>159</sup> and Sm<sub>0.5</sub>Ca<sub>0.5</sub>MnO<sub>3</sub><sup>160</sup>. In many of the studies a STO substrate was used<sup>9,32,150,151,154,160</sup>, while sometimes also other substrates such as LAO<sup>32</sup> and BaTiO<sub>3</sub> (BTO)<sup>154</sup> were reported. The role of the substrate in the results is here solely attributed to the strain it applies on the manganite layer. Lanthanum-based oxides ordering in a perovskite structure on a STO substrate resemble on the first glance the LAO/STO samples discussed in the previous section in terms of the 2DEGs. The difference is that LAO is a non-magnetic isolator, where magnetism and transport are only occurring at the interface with the substrate.

The AMR is usually reported to be two-fold, however also four-fold AMR was reported. While the four-fold symmetry was reported to be robust in La<sub>2/3</sub>Ca<sub>1/3</sub>MnO<sub>3</sub><sup>9</sup>, it only appeared on a tensile strained La<sub>0.4</sub>Sr<sub>0.6</sub>MnO<sub>3</sub> sample on a STO substrate<sup>157</sup>. Other substrates showed two-fold AMR for the same material. Arguably the most attention was paid to ferromagnetic LCMO (with X=La, Y=Ca and  $a, b$  in 2 : 1 ratio) where the colossal magnetoresistance (CMR) occurs, and here, the AMR at low temperatures<sup>154</sup> is clearly observable but small. At higher temperatures a peak was found in slightly off-stoichiometric LCMO, La<sub>0.7</sub>Ca<sub>0.3</sub>MnO<sub>3</sub> films<sup>151</sup>. In the former case<sup>154</sup> it was ascribed to be due to strain from the BTO substrate.

The sign of the AMR is in most cases predominantly negative. However, there are studies which report a sign change of the AMR as a function of temperature<sup>32,152,158,160</sup> and others which report exclusively negative results<sup>150,155</sup>. In the study of Xie *et al.*<sup>154</sup>, a 80 nm thick-sample on a BTO substrate was reported to show a sign change, while the other samples are solely negative. The sign change of the AMR was sometimes linked to a change of the easy axis with temperature.

Magnitudes of the AMR ratio are scattered between approx. 0.1% in LCMO<sup>150</sup> and 'colossal' values in excess of 100% for La<sub>0.3</sub>Pr<sub>0.4</sub>Ca<sub>0.3</sub>MnO<sub>3</sub> at its peak value approx. below 150 K<sup>32</sup> on a STO substrate as can be seen in Fig. 15(a). AMR values were reported highly sensitive to e.g. sample composition, type of substrates<sup>32</sup> - and thus strain - and current directions<sup>150</sup>. An example of the dependence of AMR on the substrate and the doping levels

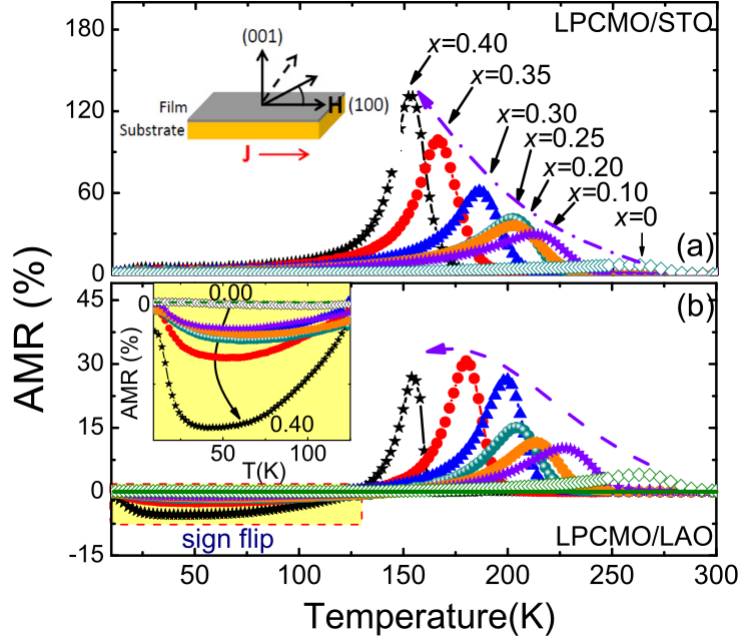


FIG. 15: AMR in  $\text{La}_{0.7-x}\text{Pr}_x\text{Ca}_{0.3}\text{MnO}_3$ . Temperature dependence of AMR measured in a field of 1.1 T at doping levels  $x = 0, 0.10, 0.20, 0.25, 0.30, 0.35,$  and  $0.40$  for films grown on (a)  $\text{SrTiO}_3$  and (b)  $\text{LaAlO}_3$  substrates. Dashed curves in both figures show the expected dependence of the  $\text{AMR}_{max}$  on doping. The change of sign of the AMR with an increasing doping is shown in the rectangular yellow area. Insets in (a) and (b) show the direction of magnetic field  $H$  and the direction of the current  $J$ , and the expanded view of the AMR at low temperatures for LPCMO/LAO doped films, respectively. The figure is reproduced from Ref.<sup>32</sup>

is shown in Fig. 15.

In an absolute majority of the studies, the low-temperature AMR increased with increasing temperature in clear contrast to the usual behavior and peaked just below the metal-insulator transition temperature. Above this temperature, the AMR ratio decreased rapidly. Microscopic mechanism of AMR in these materials is clearly distinct<sup>156</sup> from that in conventional ferromagnets (such as alloys of transition metals discussed previously). These temperatures are scattering from low temperatures<sup>155</sup> up to almost room temperature<sup>152</sup>, however usually somewhat lower than the latter. Exceptions to the high temperature peak are rare and occur for example in thin-film samples of LCMO on a BTO substrate<sup>154</sup>, in  $\text{La}_{0.4}\text{Sr}_{0.6}\text{MnO}_3$ <sup>157</sup> and in a polycrystalline  $\text{Nd}_{0.51}\text{Sr}_{0.49}\text{MnO}_3$  sample<sup>159</sup>, while the single-crystalline samples of the latter show the characteristic peak.

The explanation for the characteristic behavior is usually linked to strain resulting in orbital deformation via the Jahn-Teller effect<sup>32,151,157,158,160</sup>. While other authors offered explanations linked to double exchange<sup>154</sup> or to a magnetic liquid behavior<sup>155</sup>.

It is worth noting that the 'colossal' peak values of AMR can be usually observed in the vicinity of the MIT-temperature, where also the CMR effect occurs. Thus, explanations of these large AMR values have to be taken with some caution as neither the CMR effect is fully understood itself. In the latter case mainly due to a lack of quantitative theory describing the MIT and the subsequent insulating phase, which in our judgement might be problematic in the description of the AMR as well.

*Other conductive oxides.* In  $\text{Fe}_3\text{O}_4$  (magnetite), AMR was used to refute predicted half-metallicity<sup>30</sup> and later, a strong crystalline contribution was reported<sup>161</sup>. The origin of two- and four-fold AMR in Magnetite was linked to magnetic anisotropy and to scattering far away and near the antiphase boundaries, respectively. This oxide can be alloyed with nickel while still remaining conductive: AMR in  $\text{Ni}_{0.3}\text{Fe}_{2.7}\text{O}_4$  shows a strong four-fold component as well<sup>161</sup>. Another example of a conducting oxide is the AFM  $\text{RuO}_2$ . Here, angle-dependent spin-torque ferromagnetic resonance measurements (ST-FMR) in Fig. 3b and d of<sup>162</sup> resemble AMR and indicate the existence of the effect in the material.

#### IV. APPLICATIONS AND FURTHER TOPICS

There is a broad range of opportunities to exploit the AMR and also, to go beyond magnetisation-controlled DC resistance. In the following we will shortly discuss both industrial and scientific applications of this effect, ranging from the well-known hard-disk read heads in pre-GMR era to subtle techniques for detection of spin relaxation in ferromagnets. Related phenomena in optics and thermoelectricity will be mentioned.

##### A. Scientific applications

Since AMR gives the dependence of the resistivity on the magnetization direction, it can be used as a means of *magnetometry*. This is the main application of AMR in a scientific context and a few examples are given in the following paragraph. The second paragraph

of this section summarizes a variety of other applications of AMR measurements and theory.

A new ferromagnetic resonance (FMR) method using AMR was developed by Fang *et al.*<sup>163</sup>. There, an electrical current at microwave frequencies is used to induce an effective magnetic field in nanoscale bars of (Ga,Mn)As and (Ga,Mn)(As,P), which is then probed by voltage measurements and analyzed within the framework of non-crystalline AMR<sup>163</sup>. Comparable techniques were employed in order to detect room-temperature spin-orbit torques in the half-Heusler compound NiMnSb<sup>119</sup> and room-temperature spin-transfer torques in a structure consisting of the topological insulator Bi<sub>2</sub>Se<sub>3</sub> and permalloy<sup>164</sup>.

In another context, the AC susceptibility of thin-films of Co, Ni and Nickel alloys was determined by voltage measurements. The expression for the susceptibility (Eq. 6 in Ref.<sup>165</sup>) was derived using the non-crystalline AMR<sup>165</sup>.

And lastly, magnetization reversal was studied by AMR (amongst other means) in Nickel nanowires<sup>166</sup>. However here, the term AMR refers resistance measurements being subject to magnetic field sweeps at different field directions. Jumps in the resistance signal are taken as indication of pinning and unpinning of the magnetic domain walls in the magnetization reversal process. Comparable works can be found in Refs.<sup>35,167,168</sup>. A similar study, however with focus on detecting and characterizing the domain wall itself can be found in Ref.<sup>169</sup>.

A central ingredient of the AMR theory is the sd-scattering, which has been mentioned in many positions in this work already. Usually, theoretical predictions of the strength of sd-scattering leading to predictions about the AMR. The opposite is however also possible: A very small non-crystalline AMR of 0.001% was used to argue that sd-scattering is repressed, the electron carriers and Fermi level reside in the conduction band and the main scattering process is s-s-scattering<sup>48,170</sup>.

While the sd-scattering is governing AMR, its reverse process the  $d \rightarrow s$  electron-scattering, is involved in *spin relaxation*. A spin-relaxation theory suitable for nickel- and cobalt-based alloys based on the theory of AMR of Campbell, Fert and Jaoul<sup>55,171</sup> was developed by Berger and exemplified on permalloy. Parameters of the model were deduced from existing AMR data<sup>172</sup>.

The angular dependence of AMR was used in various occasions: First, in quantifying the current-induced Rashba fields in LAO/STO heterostructures and investigate their de-

pendence on applied magnetic field and on electric field modulation<sup>173</sup>. The LAO/STO heterostructures forming a 2DEG, which is more extensively discussed in Sec. 3 III E.

Secondly, the signals of inverse spin Hall effect (ISHE) and of AMR are typically mixed and thus knowledge about AMR is crucial to quantify the spin-Hall angle correctly. In Refs.<sup>174,175</sup> methods are shown how to unwind their signals by symmetry. The ISHE was investigated in permalloy/Pt bilayers<sup>174</sup> and in Pt, Au and Mo<sup>175</sup>, respectively.

AMR can be used to probe the dimensionality of the Fermi surface as was for example done for  $\text{Ca}_{0.73}\text{La}_{0.27}\text{FeAs}_2$  single crystals, where a quasi two-dimensionality of its Fermi surface was found<sup>176</sup>.

## B. Unconventional Examples and Related Effects

This section attempts to give a short overview on AMR-related research outside the mainstream, such as the investigation of AMR in non-collinear systems (see sec. IV B 3) where no single spin direction can be defined as in ferromagnets (net magnetization) or in collinear antiferromagnets (Néel vector); as well as discussion of similar effects which can partly make use of AMR terminology as such its thermoelectrical counterpart, the Anisotropic Magnetothermopower discussed in sec. IV B 2.

### 1. Frequency-dependent AMR

This review focuses on AMR in the DC regime. Conductivity is, nevertheless, a function of frequency  $\sigma(\omega)$  and so is its anisotropy. It is meaningful to divide the following discussion into low and higher frequencies. Given the typical scattering rates  $1/\tau$  in electrically conducting materials, the former means terahertz while the latter spans the visible range and beyond. In the following paragraph, we discuss AMR in the terahertz regime.

The special aspect of the terahertz range is that  $\sigma(\omega)$  is dominated by the intraband contributions which are usually well approximated by the Drude peak,  $\sigma(\omega) \propto (1 - i\omega\tau)^{-1}$  where  $\tau$  is the transport relaxation time. It is then possible to split<sup>12,177</sup> AMR into

$$AMR = \frac{\sigma_{\perp} - \sigma_{\parallel}}{\sigma_{\perp}} = \frac{A}{1 - i\omega\tau} + B \quad (16)$$

Since the  $\omega$ -independent term  $B$  happens to be a function of the intrinsic AMR and the  $\omega$ -dependent part of the extrinsic AMR, the ac-AMR offers a possibility for experimentally distinguish these two quantities (see sec. 1IA and 3III A)<sup>12</sup>. In these fashion, Co, Ni, Ni<sub>50</sub>Fe<sub>50</sub><sup>12</sup> and permalloy<sup>12,177</sup> were investigated (see sec. 1III A for the discussion). Please note, that the frequency-dependence was not investigated by means of AC measurements, but instead by means of radiation: The samples were subjected to an incident polarized electrical pulse in THz frequency and the after transmitting through the sample, the outgoing pulse was detected<sup>12,177</sup>.

Beyond the THz range, interband terms become important, see Eq. B6 in Ref.<sup>178</sup>. At these higher frequencies ( $\omega\tau \gg 1$ ), the focus turns to magneto-optical effects which are even in magnetization, such as the Voigt effect or its analogy in reflection (see Fig. 2 in that reference for an overview) as counterparts to AMR in the DC-limit. Spectral measurements than provide information about valence band structure: iron<sup>179</sup>, (Ga,Mn)As<sup>178</sup> or Heusler compounds<sup>180</sup>. Beyond visible and UV region, core levels can also be probed using x-ray magnetic linear dichroism (XMLD)<sup>181</sup> but these effects go beyond the scope of this review.

## 2. Anisotropic Magnetothermopower

The Anisotropic Magnetothermopower (AMTP) is the thermoelectric counterpart of the AMR. Among linear response coefficients

$$\begin{aligned} j &= eL_{11}E + L_{12}\nabla T \\ j_Q &= eL_{21}E + L_{22}\nabla T \end{aligned}$$

it is not only  $L_{11} = \sigma/e$  that may depend on magnetization direction<sup>182</sup>. Off-diagonal terms of the  $L_{12}$  tensor correspond to the Anomalous Nernst Effect (named in analogy to the anomalous Hall effect manifested in off-diagonal terms of  $L_{11}$ ), and the AMR (in  $L_{11}$ ) has the AMTP as its counterpart in  $L_{12}$ . Magnetoanisotropy of all these coefficients can be anticipated<sup>183</sup>; they are tensors bound by Onsager relations<sup>184</sup>.

Literature is sparse since measurements and calculations are both challenging. The measurements of  $L_{12}$  are challenging due to possible unwanted thermoelectric contributions which hardly can be averaged-out<sup>10</sup>. In case of the calculations, the challenge lies at

properly evaluating the derivatives,  $L_{12} \sim \int v_k^2 \delta'(E_k - E_F)$ . In the following, we provide a summary of important literature published on AMTP.

Quantitative studies based on phenomenological symmetry-based models analogous to the approach presented in sec. 2II A are conducted in  $\text{Co}_2\text{MnGa}$ <sup>10</sup> and in  $(\text{Ga,Mn})\text{As}$ <sup>7</sup>. While in  $\text{Co}_2\text{MnGa}$  only crystalline and non-crystalline AMTP components up to the second order were confirmed, higher order components have been identified in  $(\text{Ga,Mn})\text{As}$ . In both cases, AMR and AMTP components were not directly related. A further summary of AMTP studies in  $(\text{Ga,Mn})\text{As}$  can be found in sec. III - D - 2 of the review by Jungwirth *et al.*<sup>185</sup>.

Concerning the  $L_{22}$  coefficient, the AMR was compared by Kimling *et al.* to *anisotropic magnetothermal resistance effect (AMTR)* in polycrystalline Ni nanowires<sup>186</sup> for a range of temperatures. The AMR and AMTR are expressed as ratios and the AMTR is found to be weaker than the AMR due to electron-magnon-scattering. A two-current model for AMTP in analogy to the work of Campbell, Fert and Jaoul on AMR<sup>55,171</sup> was derived by Heikkilä *et al.*, see Ref.<sup>187</sup>.

### 3. Non-collinear systems

For a long time, the AMR was only associated with ferromagnets. However, the discovery of AMR in collinear antiferromagnets as described in sec. 3III C, demonstrated that AMR can also occur in other magnetically ordered materials. Collinear AFM have two sublattices (typically denoted as *spin up* and *spin down*) which are aligned parallel to each other and allow for the definition of a single spin axis (the Néel vector); practical differences between these two cases, compare the SW1 and SW2 models discussed in Sec. 1(e), are small nevertheless. Collinear AFMs alone, however, do not exploit the set of zero-net-magnetisation systems to the fullest. In case of non-collinear antiferromagnets, all magnetic moments do point in the same plane, however it is not possible to define a singular spin axis as the Neel vector. An example is magnetic ordering on a kagome lattice in  $\text{Mn}_3\text{Sn}$ <sup>42</sup> or on a trigonal lattice in  $\text{CrSe}$ <sup>188</sup>. In the latter case, magnetic moments do not lie in the same plane and such non-coplanar magnetic order can bring about unexpected consequences.

Ever since the work of McGuire and Potter<sup>1</sup>, it has been generally accepted that AMR is an effect relying on the SOI. This is however only true in collinearly ordered structures. A

non-collinear or non-coplanar order can mimic some properties of the SOI as, for example, it was shown for AHE on a distorted fcc lattice endowed with non-coplanar magnetic order<sup>189</sup>.

Now, with AMR, non-collinear order is sufficient as we demonstrate in Fig. 16: an s-d model on kagome lattice<sup>190</sup> yields an isotropic band structure as evidenced by Fermi surface (FS) in panel (b) for a symmetric ( $\alpha = 0$ ) configuration of magnetic moments. We stress that hexagonal warping (when appreciable) does not break the isotropy in the sense of  $\sigma_{xx} = \sigma_{yy}$  as discussed in Sec. 2(c). Fig. 16(d) shows that for  $\alpha \neq 0$  this symmetry is broken and this then leads to intrinsic AMR even in the absence of SOI. Note that anisotropies in scattering could result in additional extrinsic AMR.

Please note that, the definition of AMR could differ between various sources due to the lack of a single spin axis. Some people argue that AMR in non-collinear systems should be due to the simultaneous rotation of all magnetic moments. However this definition is problematic since firstly, the simultaneous rotation of all moments will not change the fermisurface symmetry and thus not allow for any effect and secondly, the application of a magnetic field will not rotate all moments simultaneously. The direction of magnetic moments after application of a magnetic field will be determined by a Stoner-Wohlfarth model SW3, as discussed in sec. 11 E.

#### 4. Exotic Phenomena

In the context of anisotropic magnetotransport, research focuses mostly on the diffusive regime in bulk systems. In the following, we wish to mention several phenomena outside this realm First, AMR in the ballistic transport regime is discussed, followed by a quick look at tunneling anisotropic magnetoresistance (TAMR) and AMR in topological insulators.

Transport in the diffusive regime is dominated by scattering, described by the mean-free path of the carrier. When the sample size becomes smaller than the mean-free path we are talking of the ballistic regime: Carriers are only scattered at the boundaries of the sample and can otherwise travel unhindered. Ballistic transport is often times related to one dimensional structures as nanowires. It is possible to have AMR in this regime, which is subsequently either called *ballistic AMR*<sup>191</sup> (BAMR) or *quantized AMR* (QAMR) because of

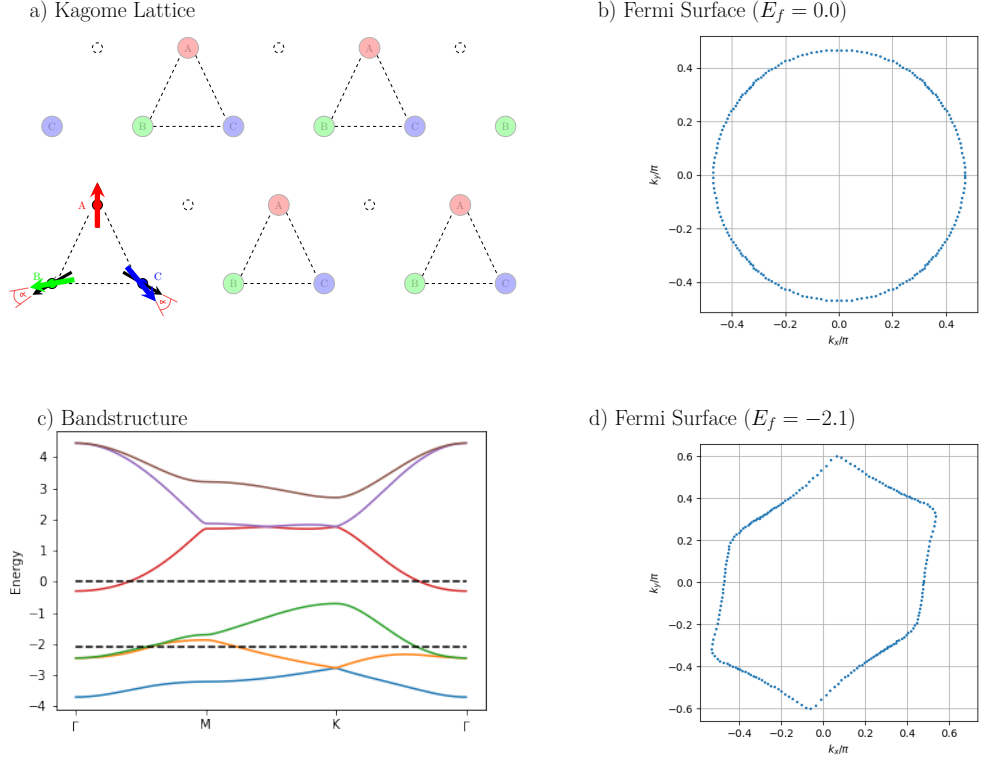


FIG. 16: Archetypal non-collinear system: kagome lattice with three MSLs. (a) Configuration of magnetic moments where (b,d) anisotropy occurs depending on  $\alpha$ . (c) Band structure with Fermi level indicated.

its stepwise character<sup>192</sup>. The BAMR is an effect similar to intrinsic AMR since in both cases no external scattering is responsible for the effect. In case of BAMR, the number of bands at the Fermi level and thus the ballistic transport changes with the magnetization direction<sup>191</sup>. It was found that the BAMR is a step function with the magnetization angle<sup>191,192</sup>. The

step-like behavior is only found at low temperatures and for small sample sizes. Increasing the size changes the number of conduction channels and leads to smearing out of the step. An increase of temperature likewise smears out the step<sup>192</sup>. In the latter cases, nickel<sup>191</sup> and iron<sup>191,192</sup> have been investigated.

The dependence of ballistic AMR on in an ideal infinite monoatomic iron wire were compared to influences of domain walls and contacts, both of which can alter the transport properties significantly<sup>193</sup>. And lastly, AMR in a Rashba 2DEG was compared between the diffusive and the ballistic regime. The diffusive AMR can be large at low carrier densities which was attributed to the dependence of density of states, while the ballistic AMR shows a nonlinear dependence on the exchange, which was attributed to Fermi-surface circle effects<sup>61</sup>.

Tunneling AMR (TAMR) can be understood as a crossover of AMR, where the anisotropy, thus changing of resistivity with magnetization direction, is important; and the Tunneling Magnetoresistance (TMR)<sup>194,195</sup>, which is based on tunneling as encrypted in its name. Seminal work by Gould *et al.*<sup>196</sup> carried out on a structure of a ferromagnetic (Ga,Mn)As layer, a tunneling barrier and a non-magnetic material attributed the anisotropy to the anisotropy of the partial DOS<sup>196</sup>. Since then, TAMR has remained a current topic. Recently, Schöneberg *et al.*<sup>197</sup>, found that Pb dimers on a ferromagnetic surface show different results depending on the crystalline orientation. For a [001]-oriented dimer, the TAMR reached up to 20%, linked to a difference of LDOS depending on the magnetization direction, while TAMR is absent for a [111]-orientation due to only small difference of LDOS depending on magnetization<sup>197</sup>. The TAMR is very much a topic of its own, only related by analogy to the original AMR effect and further discussion is beyond the scope of this review.

Kandala *et al.*<sup>198</sup> found that in the Cr-doped topological insulator (Bi,Sb)<sub>2</sub>Te<sub>3</sub>, which is a FM up to 8 K, exhibits a giant AMR of more than 120% in an rotation from out-of-plane to in-plane. This is, because for out-of-plane field, a magnetic gap opens for the surface states (quantum AHE), but when the field is in-plane, surface states are restored<sup>198</sup>.

### C. Industrial Applications

Arguably the best-known applications of AMR fall into the realm of magnetic memories. Early Magnetoresistive Random Access Memories (MRAM) were based on the effect, yet it is much smaller in magnitude than GMR which eventually prevailed. Modern MRAMs are based on the TMR effect<sup>199</sup>. To date, AMR is still used in applications related to the conventional hard drives<sup>199</sup> where information is read using a multilayer device<sup>200,201</sup> whose resistance changes depending on the magnetic state of the free layer. In the recent decade, numerous attempts of developing novel spintronic applications based on antiferromagnets (see sec. 3III C) were made. In the proposed applications, AMR and its transversal counterpart the planar Hall effect (PHE) were considered as a readout mechanism<sup>36,105,109</sup>. To date, AFM spintronic applications did not reach to market readiness.

Sensors based on the AMR effect are nowadays still widely used in applications including detection of absolute position and angle or rotation speed<sup>201-203</sup>. Important is the usage in the automotive industry, for example in sensing of crank shaft position, wheel and transmission speed, throttle valve position for air intake and many more<sup>204</sup>. A list of further applications can be found in the beginning of Ref.<sup>204</sup>. Further examples include weak field measurements<sup>203</sup> such as in a compass<sup>205</sup>, traffic detection and measurements of current<sup>203,206</sup>. The measurements of current are taking advantage of Ampere's Law where the AMR sensors detect the magnetic field induced by a current flowing through a wire<sup>206</sup>. AMR sensors offer quite a few advantages, which explains their popularity in industrial applications. They can be produced at low cost<sup>200,202,204</sup>, are quite small<sup>202</sup>, achieve a high sensitivity<sup>202,203</sup> with resolution well below millimeter or degree-range and are still working if there is a gap between sensor and magnet<sup>202</sup> to name only a few. In comparison to Hall sensors they convince with a higher sensitivity<sup>206</sup>, lower cost and less sensitivity to mechanical stress<sup>204</sup>.

Requirements for materials used in AMR sensors include large AMR signal (high signal to operating voltage ratio), large  $\rho_0$  (noise reduction), low anisotropy, low sensitivity to magnetostriction, long-term stability<sup>203</sup>. Wide temperature ranges are required for operation in e.g. automotive applications as temperature can vary by more than 100°C. A linear temperature dependence can be compensated electronically<sup>204</sup>. Commonly used materials are

mainly basic transition metals discussed in sec.3III A and especially permalloy<sup>200,203,207</sup>. The latter has many of the desired properties.

In application-based publications the AMR is identified as non-crystalline AMR<sup>200,202,203</sup>, treatments of crystalline components are to our knowledge not present. The noise in AMR sensors is typically dominated by magnetic fluctuations<sup>201</sup>. Please note that similar to AMR sensors, the transverse Planar Hall effect (PHE) can be used to fabricate PHE sensors<sup>207</sup>.

## V. CONCLUSION

Magnetotransport in solids is a vast and mature field. In this review, we focus only on a small part of it, namely its anisotropy related to magnetic order. The anisotropic magnetoresistance (AMR) usually refers to this phenomenon albeit occasionally, orbital effects are also included (and these are not covered in this review). Two characteristic features of magnetism are helpful to this end: remanence and coercivity. Unlike ordinary magnetoresistance which just happens to be anisotropic, the AMR can usually be observed as a spontaneous effect even at zero field; on the other hand, well above coercive field, magnetoresistance traces should run in parallel regardless of the experimental configuration (e.g. magnetic field parallel and perpendicular to current). Microscopically, the AMR can either originate from anisotropic scattering or band structure deformation (related to magnetic order) which is analogous to the extrinsic and intrinsic mechanism of the anomalous Hall effect (AHE). This analogy is not very deep, however, as it can be exemplified with the intrinsic AMR which is unrelated to Berry curvature of Bloch states.

Phenomenological understanding of the AMR is based on symmetry analysis (of resistivity tensor) and the basic distinction of non-crystalline, Eq. 1.2, and crystalline (or mixed) terms allows to distinguish single crystals from polycrystals where only the former occurs. Absolute and relative values of the AMR coefficient in Eq. 1.2, as a material parameter, are useful for polycrystals and single crystals, respectively. While the latter is usually used, one should be careful: sputtered films of the same material will exhibit different relative AMR depending on the strength of scattering on grain boundaries (which is typically unrelated to magnetism). Strong variations of published AMR values are therefore to be expected.

While the AHE has attracted considerably more attention than AMR in fundamental research, situation is quite the opposite in commercial applications. Contrary to AHE,

the AMR has already made it to the market-ready stage in the niche of various sensors (spintronic memories, traffic detection and more) and also scientific applications of AMR (such as a means to determine magnetisation direction in situations where other methods fail) have become important. More work is needed, however, to close the gap between real-world applications and the large body of fundamental research that has been carried out on AMR over last 165 years.

---

\* Electronic address: ritzinger@fzu.cz, vybornyk@fzu.cz

- <sup>1</sup> McGuire T, Potter T. 1975. Anisotropic magnetoresistance in ferromagnetic 3d alloys. *IEEE Trans Mag* **11**, 18. (doi: 10.1109/TMAG.1975.1058782)
- <sup>2</sup> Isnaini VA, Kolonits T, Czigány Zs, Gubicza J, Zsurzsa S, Varga LK, Tóth-Kádár E, Pogány L, Péter L, Bakonyi I. 2020. Room-temperature magnetoresistance of nanocrystalline Ni metal with various grain sizes. *Eur. Phys. J. Plus* **135**:39. (doi: 10.1140/epjp/s13360-019-00067-2)
- <sup>3</sup> Thomson W. 1857. XIX. On the electro-dynamic qualities of metals:—Effects of magnetization on the electric conductivity of nickel and of iron. *Proc. Roy. Soc. London* **8**, 546. (doi: 10.1098/rspl.1856.0144)
- <sup>4</sup> Thomlinson H. 1882. IV. The influence of stress and strain on the action of physical forces. *Proc. Roy. Soc. London* **33**, 276. (doi: 10.1098/rspl.1881.0108)
- <sup>5</sup> Döring W. 1938. Die Abhängigkeit des Widerstandes von Nickelkristallen von der Richtung der spontanen Magnetisierung *Ann. Phys.* **5**, 259. (doi: 10.1002/andp.19384240306)
- <sup>6</sup> De Ranieri *et al.* 2008. Lithographically and electrically controlled strain effects on anisotropic magnetoresistance in (Ga,Mn)As *New J. Phys.* **10**, 065003. (doi: 10.1088/1367-2630/10/6/065003)
- <sup>7</sup> Althammer M. 2012. Spin-transport-phenomena in metals, semiconductors, and insulators. [Ph.D Thesis]. München, Technische Universität München.
- <sup>8</sup> Limmer W, Glunk M, Daeubler J, Hummel T, Schoch W, Sauer R, Bihler C, Huebl H, Brandt MS, Goennenwein STB. 2006. Angle-dependent magnetotransport in cubic and tetragonal ferromagnets: Application to (001)- and (113)A-oriented (Ga,Mn)As *Phys. Rev. B* **74**, 205205. (doi: 10.1103/PhysRevB.74.205205)
- <sup>9</sup> Li J, Li SL, Wu ZW, Li S, Chu HF, Wang J, Zhang Y, Tian HY, Zheng DN. 2010. A phenomenological approach to the anisotropic magnetoresistance and planar Hall effect in tetragonal  $\text{La}_{2/3}\text{Ca}_{1/3}\text{MnO}_3$  thin films *J. Phys.: Condens. Matter* **22**, 146006. (doi: 10.1088/0953-8984/22/14/146006)
- <sup>10</sup> Ritzinger P *et al.* 2021. Anisotropic magnetothermal transport in  $\text{Co}_2\text{MnGa}$  thin films *Phys. Rev. B* **104**, 094406 (doi: 10.1103/PhysRevB.104.094406)
- <sup>11</sup> Zeng FL, Ren ZY, Li Y, Zeng JY, Jia MW, Miao J, Hoffmann A, Zhang W, Wu YZ, Yuan

- Z. 2020. Intrinsic Mechanism for Anisotropic Magnetoresistance and Experimental Confirmation in  $\text{Co}_x\text{Fe}_{1-x}$  Single-Crystal Films. *Phys. Rev. Lett.* **125**, 097201. (doi: 10.1103/PhysRevLett.125.097201)
- <sup>12</sup> Nádvořník L *et al.* 2021. Broadband Terahertz Probes of Anisotropic Magnetoresistance Disentangle Extrinsic and Intrinsic Contributions. *Phys. Rev. X* **11**, 021030. (doi: 10.1103/PhysRevX.11.021030)
- <sup>13</sup> L.F. Bates 1946. The magneto-resistance of high coercivity alloys. *Proc. Phys. Soc.* **58**, 153. (doi: 10.1088/0959-5309/58/2/302)
- <sup>14</sup> Mott NF. 1964. Electrons in transition metals. *Adv. Phys.* **13**, 325. (doi: 10.1080/00018736400101041)
- <sup>15</sup> Kokado S, Tsunoda M, Harigaya K, Sakuma A. 2012. Anisotropic Magnetoresistance Effects in Fe, Co, Ni,  $\text{Fe}_4\text{N}$ , and Half-Metallic Ferromagnet: A Systematic Analysis. *J. Phys. Soc. Jpn.* **81**, 024705. (doi: 10.1143/JPSJ.81.024705)
- <sup>16</sup> Rushforth AW *et al.* 2007. Anisotropic Magnetoresistance Components in  $(\text{Ga,Mn})\text{As}$ . *Phys. Rev. Lett.* **99**, 147207. (doi: 10.1103/PhysRevLett.99.147207)
- <sup>17</sup> Výborný K, Kučera J, Sinova J, Rushforth AW, Gallagher BL, Jungwirth T. 2009. Microscopic mechanism of the noncrystalline anisotropic magnetoresistance in  $(\text{Ga,Mn})\text{As}$ . *Phys. Rev. B* **80**, 165204. (doi: 10.1103/PhysRevB.80.165204)
- <sup>18</sup> Yang FJ, Sakuraba Y, Kokado S, Kota Y, Sakuma A, and Takanashi K. 2012. Anisotropic magnetoresistance in  $\text{Co}_2(\text{Fe,Mn})\text{Si}$  Heusler epitaxial films: A fingerprint of half-metallicity. *Phys. Rev. B* **86**, 020409 (R). (doi: 10.1103/PhysRevB.86.020409)
- <sup>19</sup> Sato T, Kokado S, Kosaka S, Ishikawa T, Ogawa T, Tsunoda M. 2018. Large negative anisotropic magnetoresistance in  $\text{Co}_2\text{MnGa}$  Heusler alloy epitaxial thin films. *Appl. Phys. Lett.* **113**, 112407. (doi: 10.1063/1.5047821)
- <sup>20</sup> Sato T, Kokado S, Tsujikawa M, Ogawa T, Kosaka S, Shirai M, Tsunoda M. 2019. Signs of anisotropic magnetoresistance in  $\text{Co}_2\text{MnGa}$  Heusler alloy epitaxial thin films based on current direction. *Appl. Phys. Express* **12**, 103005. (doi: 10.7567/1882-0786/ab42b4)
- <sup>21</sup> Miao Y, Yang D, Jia L, Li X, Yang S, Gao C, Xue D. 2021. Magnetocrystalline anisotropy correlated negative anisotropic magnetoresistance in epitaxial  $\text{Fe}_{30}\text{Co}_{70}$  thin films. *Appl. Phys. Lett.* **118**, 042404. (doi: 10.1063/5.0034232)
- <sup>22</sup> Kabara K, Tsunoda M, Kokado S. 2017. Magneto-transport properties of pseudo-single-crystal

- Mn<sub>4</sub>N thin films *AIP Advances* **7**, 056416. (doi: 10.1063/1.4974065)
- <sup>23</sup> Yang FJ, Wei C, Chen XQ. 2013. Half-metallicity and anisotropic magnetoresistance of epitaxial Co<sub>2</sub>FeSi Heusler films *Appl. Phys. Lett.* **102**, 172403. (doi: 10.1063/1.4803537)
- <sup>24</sup> Kabara K, Tsunoda M, Kokado S. 2016. Transverse anisotropic magnetoresistance effects in pseudo-single-crystal  $\gamma'$ -Fe<sub>4</sub>N thin films. *AIP Advances* **6**, 055818. (doi: 10.1063/1.4943923)
- <sup>25</sup> Omori Y, Sagasta E, Niimi Y, Gradhand M, Hueso LE, Casanova F, Otani YC. 2019. Relation between spin Hall effect and anomalous Hall effect in 3d ferromagnetic metals *Phys. Rev. B* **99**, 014403. (doi: 10.1103/PhysRevB.99.014403)
- <sup>26</sup> Pippard AB. 1989. Magnetoresistance in Metals (Cambridge Studies in Low Temperature Physics, Series Number 2). Cambridge University Press. (ISBN 10: 0521118808)
- <sup>27</sup> Zhang SN, Wu QS, Liu Y, Yazyev OV. 2019. Magnetoresistance from Fermi surface topology. *Phys. Rev. B* **99**, 035142. (doi: 10.1103/PhysRevB.99.035142)
- <sup>28</sup> Ebert H, Vernes A, Banhart J. 1996. Anisotropic electrical resistivity of ferromagnetic Co-Pd and Co-Pt alloys. *Phys. Rev. B* **54**, 8479. (doi: 10.1103/PhysRevB.54.8479)
- <sup>29</sup> Stampe PA, Kunkel HP, Wang Z, Williams G. 1995. Influence of spin-orbit coupling on the transport and magnetic properties of Co<sub>3</sub>Pd<sub>97</sub>. *Phys. Rev. B* **52**, 335. (doi: 10.1103/PhysRevB.52.335)
- <sup>30</sup> M. Ziese. 2000. *Phys. Rev. B* **62**, 1044. (doi: 10.1103/PhysRevB.62.1044)
- <sup>31</sup> Chakraborty S, Majumdar AK. 1998. Galvanomagnetic studies in  $\gamma$ -Ni<sub>100-x-y</sub>Fe<sub>x</sub>Cr<sub>y</sub> permalloys ( $x, y \sim 10\%$ ). *Phys. Rev. B* **58**, 6434. (doi: 10.1103/PhysRevB.58.6434)
- <sup>32</sup> Alagoz HS, Desomberg J, Taheri M, Razavi FS, Chow KH, Jung J. 2015. Mechanism of sign crossover of the anisotropic magneto-resistance in La<sub>0.7-x</sub>Pr<sub>x</sub>Ca<sub>0.3</sub>MnO<sub>3</sub> thin films. *Appl. Phys. Lett.* **106**, 082407. (doi: 10.1063/1.4913875)
- <sup>33</sup> M. El-Tahawy et al. 2022. *J. Magn. Magn. Mat.* **560**, 169660. (doi: 10.1016/j.jmmm.2022.169660)
- <sup>34</sup> Mizusaki S, Ohnishi T, Douzono A, Nagata Y, Ozawa TC, Samata H, Noro Y. 2009. Large anisotropic magnetoresistance of ruthenium-based Heusler alloy. *J. Appl. Phys.* **105**, 07E513. (doi: 10.1063/1.3080561)
- <sup>35</sup> Bolte M, Steiner M, Pels C, Barthelmeß M, Kruse J, Merkt U, Meier G, Holz M, Pfannkuche D. 2005. Magnetotransport through magnetic domain patterns in permalloy rectangles. *Phys. Rev. B* **72**, 224436. (doi: 10.1103/PhysRevB.72.224436)

- <sup>36</sup> Kriegner D. *et al.* 2016 Multiple-stable anisotropic magnetoresistance memory in antiferromagnetic MnTe. *Nat. Commun.* **7**, 11623. doi: 10.1038/ncomms11623
- <sup>37</sup> Stoner EC, Wohlfarth EP. 1948. A mechanism of magnetic hysteresis in heterogeneous alloys. *Phil. Trans. Roy. Soc. A* **240**, 826 (1948). doi: 10.1098/rsta.1948.0007
- <sup>38</sup> Volný J, Wagenknecht D, Železný J, Harcuba P, Duverger–Nedellec E, Colman RH, Kudrnovský J, Turek I, Uhlířová K, Výborný K. 2020. Electrical transport properties of bulk tetragonal CuMnAs. *Phys. Rev. Materials* **4**, 064403. doi: 10.1103/PhysRevMaterials.4.064403
- <sup>39</sup> Limmer W, Daeubler J, Dreher L, Glunk M, Schoch W, Schwaiger S, Sauer R. 2008. Advanced resistivity model for arbitrary magnetization orientation applied to a series of compressive-to tensile-strained (Ga,Mn)As layers. *Phys. Rev. B* **77**, 205210. (doi: 10.1103/PhysRevB.77.205210)
- <sup>40</sup> Song C, You Y, Chen X, Zhou X, Wang Y, Pan F. 2018. How to manipulate magnetic states of antiferromagnets. *Nanotechnology* **29** 112001. (doi: 10.1088/1361-6528/aaa812)
- <sup>41</sup> Correa C A and Výborný K 2018. *Phys. Rev. B* **97**, 235111. (doi: 10.1103/PhysRevB.97.235111)
- <sup>42</sup> Liu J, Balents L. 2017. Anomalous Hall Effect and Topological Defects in Antiferromagnetic Weyl Semimetals: Mn<sub>3</sub>Sn / Ge. *Phys. Rev. Lett.* **119**, 087202. (doi: 10.1103/PhysRevLett.119.087202)
- <sup>43</sup> Birss RR. 1966. Symmetry and magnetism, Series of monographs on selected topics in solid state physics. North-Holland Pub. Co. (doi?)
- <sup>44</sup> Ritzinger P. 2020. Magneto-thermo-galvanic Measurements in Magnetic Thin-films. [Master Thesis]. Dresden, Technische Universität Dresden.
- <sup>45</sup> Kokado S, Tsunoda M. 2015. Twofold and Fourfold Symmetric Anisotropic Magnetoresistance Effect in a Model with Crystal Field. *J. Phys. Soc. Jpn.* **84**, 094710. (doi: 10.7566/JPSJ.84.094710)
- <sup>46</sup> Kriegner D *et al.* 2017. Magnetic anisotropy in antiferromagnetic hexagonal MnTe. *Phys. Rev. B* **96**, 214418. (doi: 10.1103/PhysRevB.96.214418)
- <sup>47</sup> De Ranieri E, Rushforth AW, Výborný K, Rana U, Ahmad E, Champion RP, Foxon CT, Gallagher BL, Irvine AC, Wunderlich J. 2008. Lithographically and electrically controlled strain effects on anisotropic magnetoresistance in (Ga,Mn)As. *New J. Phys.* **10** 065003. (doi:

10.1088/1367-2630/10/6/065003)

- <sup>48</sup> Nam Hai P, Sasaki D, Duc Anh L, Tanaka M. 2012. Crystalline anisotropic magnetoresistance with two-fold and eight-fold symmetry in (In,Fe)As ferromagnetic semiconductor. *Appl. Phys. Lett.* **100**, 262409. (doi: 10.1063/1.4730955)
- <sup>49</sup> Terry I, Penney T, von Molnar S, Becla P. 1996. Low temperature magnetoresistance of the persistent photoconductor  $\text{Cd}_{0.9}\text{Mn}_{0.1}\text{Te:In}$ . *J. Cryst. Growth* **159**, 1070. (doi: 10.1016/0022-0248(95)00695-8)
- <sup>50</sup> Intrinsic anomalous Hall effect is one of the exceptions: off-diagonal conductivity component can be expressed in terms of an integral of so called Berry curvature over Fermi sea (rather than Fermi surface). For DMS, this has been done for example in Ref.<sup>208</sup>.
- <sup>51</sup> Trushin M, Výborný K, Moraczewski P, Kovalev AA, Schliemann J, Jungwirth T. 2009. Anisotropic magnetoresistance of spin-orbit coupled carriers scattered from polarized magnetic impurities. *Phys. Rev. B* **80**, 134405. (doi: 10.1103/PhysRevB.80.134405)
- <sup>52</sup> Výborný K, Kovalev AA, Sinova J, Jungwirth T. 2009. Semiclassical framework for the calculation of transport anisotropies. *Phys. Rev. B* **79**, 045427. (doi: 10.1103/PhysRevB.79.045427)
- <sup>53</sup> Ahn S, Das Sarma S. 2021. Screening, Friedel oscillations, RKKY interaction, and Drude transport in anisotropic two-dimensional systems. *Phys. Rev. B* **103**, 165303 (doi: 10.1103/PhysRevB.103.165303)
- <sup>54</sup> Smit J. 1951. Magnetoresistance of ferromagnetic metals and alloys at low temperatures. *Physica* **16** 612. (doi: 10.1016/0031-8914(51)90117-6)
- <sup>55</sup> Jaoul O, Campbell IA, Fert A. 1977. Spontaneous resistivity anisotropy in Ni alloys. *J. Magn. Magn. Mater.* **5**, 23. (doi: 10.1016/0304-8853(77)90193-7)
- <sup>56</sup> da Câmara Santa Clara Gomes T, Marchal N, Abreu Araujo F, Piraux L. 2019. Tunable magnetoresistance and thermopower in interconnected NiCr and CoCr nanowire networks. *Appl. Phys. Lett.* **115**, 242402. (doi: 10.1063/1.5130718)
- <sup>57</sup> Jungwirth T, Sinova J, Mašek J, Kučera J, MacDonald AH. 2006. Theory of ferromagnetic (III,Mn)V semiconductors. *Rev. Mod. Phys.* **78**, 809. (doi: 10.1103/RevModPhys.78.809)
- <sup>58</sup> Jungwirth T, Sinova J, Wang KY, Edmonds KW, Champion RP, Gallagher BL, Foxon CT, Niu Q, MacDonald AH. 2003. Dc-transport properties of ferromagnetic (Ga,Mn)As semiconductors. *Appl. Phys. Lett.* **83**, 320. doi: 10.1063/1.1590433
- <sup>59</sup> Trushin M, Castro Neto AH, Vignale G, Culcer D. 2019. Hidden anisotropy in the Drude

- conductivity of charge carriers with Dirac-Schrödinger dynamics. *Phys. Rev. B* **100**, 035427. (doi: 10.1103/PhysRevB.100.035427)
- <sup>60</sup> Kato T, Ishikawa Y, Itoh H, Inoue J. 2007. Magnetoresistance and Hall effect in spin-polarized two-dimensional electron gas with spin-orbit interaction. *phys. stat. sol. (b)* **244**, No. 12, 4403–4406. (doi: 10.1002/pssb.200777260)
- <sup>61</sup> Kato T, Ishikawa Y, Itoh H, Inoue J. 2008. Intrinsic anisotropic magnetoresistance in spin-polarized two-dimensional electron gas with Rashba spin-orbit interaction. *Phys. Rev. B* **77**, 233404. (doi: 10.1103/PhysRevB.77.233404)
- <sup>62</sup> Mott NF. 1936. The Electrical Conductivity of Transition Metals. *Proc. Roy. Soc.* **A153**, 699. (doi: 10.1098/rspa.1936.0031)
- <sup>63</sup> Banhart J, Ebert H. 1995. First-Principles Theory of Spontaneous-Resistance Anisotropy and Spontaneous Hall Effect in Disordered Ferromagnetic Alloys. *EPL* **32**, 517. doi: 10.1209/0295-5075/32/6/010
- <sup>64</sup> H Ebert et al 2011. *Rep. Prog. Phys.* **74**, 096501. (doi: 10.1088/0034-4885/74/9/096501)
- <sup>65</sup> Turek I, Kudrnovský J, and Drchal V. 2012. *Ab initio* theory of galvanomagnetic phenomena in ferromagnetic metals and disordered alloys. *Phys. Rev. B* **86**, 014405. (doi: 10.1103/PhysRevB.86.014405)
- <sup>66</sup> Khmelevskiy S, Palotás K, Szunyogh L, Weinberger P. 2003. *Ab initio* calculation of the anisotropic magnetoresistance in  $\text{Ni}_{1-c}\text{Fe}_c$  bulk alloys. *Phys. Rev. B* **68**, 012402. (doi: 10.1103/PhysRevB.68.012402)
- <sup>67</sup> Freitas P P, Berger L, Silvain J F 1987. *J Appl Phys* **61**, 4385. (doi: 10.1063/1.338430)
- <sup>68</sup> Šipr O, Wimmer S, Mankovsky S, Ebert H. 2020. Transport properties of doped permalloy via *ab initio* calculations: Effect of host disorder. *Phys. Rev. B* **101**, 085109. (doi: 10.1103/PhysRevB.101.085109)
- <sup>69</sup> Vernes A, Ebert H, Banhart J. 2003. Electronic conductivity in  $\text{Ni}_x\text{Cr}_{1-x}$  and  $\text{Ni}_x\text{Cu}_{1-x}$  fcc alloy systems. *Phys. Rev. B* **68**, 134404. (doi: 10.1103/PhysRevB.68.134404)
- <sup>70</sup> Yin Y *et al.* 2015. Tunable permalloy-based films for magnonic devices. *Phys. Rev. B* **92**, 024427. (doi: 10.1103/PhysRevB.92.024427)
- <sup>71</sup> Brito WH, Aguiar MCO, Haule K, Kotliar G. 2016. Metal-Insulator Transition in  $\text{VO}_2$ : A DFT+DMFT Perspective. *Phys. Rev. Lett.* **117**, 056402. (doi: 10.1103/PhysRevLett.117.056402)

- <sup>72</sup> Šmejkal L, Železný J, Sinova J, Jungwirth T. 2017. Electric Control of Dirac Quasiparticles by Spin-Orbit Torque in an Antiferromagnet. *Phys. Rev. Lett.* **118**, 106402. (doi: 10.1103/PhysRevLett.118.106402)
- <sup>73</sup> Yang H *et al.* 2021. Colossal angular magnetoresistance in the antiferromagnetic semiconductor EuTe<sub>2</sub>. *Phys. Rev. B* **104**, 214419 (doi: 10.1103/PhysRevB.104.214419)
- <sup>74</sup> Rijks TGSM, Coehoorn R, de Jong MJM, de Jonge WJM. 1995. Semiclassical calculations of the anisotropic magnetoresistance of NiFe-based thin films, wires, and multilayers. *Phys. Rev. B* **51**, 283. (doi: 10.1103/PhysRevB.51.283)
- <sup>75</sup> van Gorkom RP, Caro J, Klapwijk TM, Radelaar S. 2001. Temperature and angular dependence of the anisotropic magnetoresistance in epitaxial Fe films. *Phys. Rev. B* **63**, 134432. (doi: 10.1103/PhysRevB.63.134432)
- <sup>76</sup> Kimling J, Gooth J, Nielsch K. 2013. Anisotropic magnetothermal resistance in Ni nanowires. *Phys. Rev. B* **87**, 094409. (doi: 10.1103/PhysRevB.87.094409)
- <sup>77</sup> Xiao X, Li JX, Ding Z, Wu YZ. 2015. Four-fold symmetric anisotropic magnetoresistance of single-crystalline Ni(001) film. *J. Appl. Phys.* **118**, 203905. (doi: 10.1063/1.4936175)
- <sup>78</sup> I. Bakonyi *et al.* 2002. *Europhys. Lett.* **58**, 408.
- <sup>79</sup> Xiao X, Liang JH, Chen BL, Li JX, Ma DH, Ding Z, Wu YZ. 2015. Current-direction dependence of the transport properties in single-crystalline face-centered-cubic cobalt films. *J. Appl. Phys.* **118**, 043908. (doi: 10.1063/1.4927620)
- <sup>80</sup> Miao Y, Chen X, Yang S, Zheng K, Lian Z, Wang Y, Wang P, Gao C, Yang D-Z, Xue D-S. 2020. Non-cosine square angular-dependent magnetoresistance of the face-centered-cubic Co thin films. *J. Magn. Magn. Mater.* **512**, 167013. (doi: 10.1016/j.jmmm.2020.167013)
- <sup>81</sup> Levy P M, Fert A 2016. *C. R. Physique* **17**, 447.
- <sup>82</sup> McGuire T, Aboaf J, Klokhholm E. 1984. Negative anisotropic magnetoresistance in 3d metals and alloys containing iridium. *IEEE Trans Mag* **20**, 5. (doi: 10.1109/TMAG.1984.1063188)
- <sup>83</sup> Ishio S, Haga H, Shindo S, Saito H. 1999. Anisotropic Magnetoresistance in Fe-Co-Ni Alloys. *J. Magn. Soc. Japan* **23**, 427. doi: 10.3379/jmsjmag.23.427
- <sup>84</sup> Berger L, Freitas PP, Warner JD, Schmidt JE. 1988. On the temperature dependence of the magnetoresistance of ferromagnetic alloys. *J. Appl. Phys.* **64**, 5459. doi: 10.1063/1.342347
- <sup>85</sup> Miyazaki T, Oikawa M. 1991. Magnetoresistance of Ni-Fe-Co ternary alloy films. *J. Magn. Magn. Mater.* **97**, 171. (doi: 10.1016/0304-8853(91)90177-C)

- <sup>86</sup> Wang S, Gao T, Wang C, He J. 2013. Studies of anisotropic magnetoresistance and magnetic property of Ni<sub>81</sub>Fe<sub>19</sub> ultra-thin films with the lower base vacuum. *J. All. Comp.* **554**, 405. (doi: 10.1016/j.jallcom.2012.12.004)
- <sup>87</sup> Dahlberg ED, Riggs K. 1988. Magnetotransport: An ideal probe of anisotropy energies in epitaxial films (invited). *J. Appl. Phys.* **63**, 4270. (doi: 10.1063/1.340200)
- <sup>88</sup> Mašek J *et al.*. 2010. Microscopic Analysis of the Valence Band and Impurity Band Theories of (Ga,Mn)As. *Phys. Rev. Lett.* **105**, 227202. (doi: 10.1103/PhysRevLett.105.227202)
- <sup>89</sup> Baxter DV, Ruzmetov D, Scherschligt J, Sasaki Y, Liu X, Furdyna JK, Mielke CH. 2002. Anisotropic magnetoresistance in Ga<sub>1-x</sub>Mn<sub>x</sub>As. *Phys. Rev. B* **65**, 212407. (doi: 10.1103/PhysRevB.65.212407)
- <sup>90</sup> Wang KY, Edmonds KW, Champion RP, Zhao LX, Foxon CT, Gallagher BT. 2005. Anisotropic magnetoresistance and magnetic anisotropy in high-quality (Ga,Mn)As films. *Phys. Rev. B* **72**, 085201. (doi: 10.1103/PhysRevB.72.085201)
- <sup>91</sup> Miyakozawa S, Chen L, Matsukura F, Ohno H. 2016. Temperature dependence of in-plane magnetic anisotropy and anisotropic magnetoresistance in (Ga,Mn)As codoped with Li. *Appl. Phys. Lett.* **108**, 112404. doi: 10.1063/1.4944328
- <sup>92</sup> Howells B, Wang M, Edmonds KW, Wadley P, Champion RP, Rushforth AW, Foxon CT, Gallagher BL. 2013. Crystalline anisotropic magnetoresistance in quaternary ferromagnetic semiconductor (Ga,Mn)(As,Sb). *Appl. Phys. Lett.* **102**, 052407. doi: 10.1063/1.4791580
- <sup>93</sup> W. Wang *et al.* in RSC Adv., Effect of Sb content on anisotropic magnetoresistance in a (Ga, Mn)(As, Sb) ferromagnetic semiconductor thin film. RSC Adv. **9**, 10776. doi: 10.1039/c8ra10256b
- <sup>94</sup> Jungwirth T, Abolfath M, Sinova J, Kučera J, MacDonald AH. 2002. Boltzmann theory of engineered anisotropic magnetoresistance in (Ga,Mn)As. *Appl. Phys. Lett.* **81**, 4029. doi: 10.1063/1.1523160
- <sup>95</sup> Jungwirth T *et al.* 2005. Prospects for high temperature ferromagnetism in (Ga,Mn)As semiconductors. *Phys. Rev. B* **72**, 165204. (doi: 10.1103/PhysRevB.72.165204)
- <sup>96</sup> Shapira Y, Oliveira, Jr. NF, Becla P, Vu TQ. 1990. Magnetoresistance and Hall effect near the metal-insulator transition of n-type Cd<sub>0.95</sub>Mn<sub>0.05</sub>Te. *Phys. Rev. B* **41**, 5931. (doi: 10.1103/PhysRevB.41.5931)
- <sup>97</sup> Navarro-Quezada A, Aiglinger M, Faina B, Gas K, Matzer M, Li T, Adhikari R, Sawicki M, Bo-

- nanni A. 2019. Magnetotransport in phase-separated (Ga,Fe)N with  $\gamma'$ -Ga<sub>y</sub>Fe<sub>4-y</sub>N nanocrystals. *Phys. Rev. B* **99**, 085201. (doi: 10.1103/PhysRevB.99.085201)
- <sup>98</sup> Lee JS, Richardella A, Rench DW, Fraleigh RD, Flanagan TC, Borchers JA, Tao J, Samarth N. 2014. Ferromagnetism and spin-dependent transport in n-type Mn-doped bismuth telluride thin films. *Phys. Rev. B* **89**, 174425. (doi: 10.1103/PhysRevB.89.174425)
- <sup>99</sup> Dyck JS, Drašar Č, Lošt'ák P, Uher C. 2005. Low-temperature ferromagnetic properties of the diluted magnetic semiconductor Sb<sub>2-x</sub>Cr<sub>x</sub>Te<sub>3</sub>. *Phys. Rev. B* **71**, 115214. (doi: 10.1103/PhysRevB.71.115214)
- <sup>100</sup> Lee JW, Kuroda S, Takano F, Akinaga H, Takita K. 2006. Anisotropy of magnetization and magnetoresistance of (Zn,Co)O films grown by pulsed laser deposition. *phys. stat. sol. (c)* **3**, 4098. (doi: 10.1002/pssc.200672872)
- <sup>101</sup> Khalid M, Esquinazi P. 2012. Hydrogen-induced ferromagnetism in ZnO single crystals investigated by magnetotransport. *Phys. Rev. B* **85**, 134424. (doi: 10.1103/PhysRevB.85.134424)
- <sup>102</sup> Landau LD. 1933. A possible explanation of the field dependence of the susceptibility at low temperatures. *Phys. Z. Sowjet* **4**, 675. (doi: 10.1016/B978-0-08-010586-4.50017-1)
- <sup>103</sup> Fina I *et al.* 2014. Anisotropic magnetoresistance in an antiferromagnetic semiconductor. *Nat. Commun.* **5**, 4671. (doi: 10.1038/ncomms5671)
- <sup>104</sup> Wang C, Seinige H, Cao G, Zhou J-S, Goodenough JB, Tsoi M. 2014. Anisotropic Magnetoresistance in Antiferromagnetic Sr<sub>2</sub>IrO<sub>4</sub>. *Phys. Rev. X* **4**, 041034. doi: 10.1103/PhysRevX.4.041034
- <sup>105</sup> X. Marti *et al.* 2014. Room-temperature antiferromagnetic memory resistor. *Nature Mater.* **13**, 367. (doi: 10.1038/nmat3861)
- <sup>106</sup> Kudrnovský J, Drchal V, Turek I. 2015. Physical properties of FeRh alloys: The antiferromagnetic to ferromagnetic transition. *Phys. Rev. B* **91**, 014435. (doi: 10.1103/PhysRevB.91.014435)
- <sup>107</sup> Kabara K, Tsunoda M, Kokado S. 2014. Annealing effects on nitrogen site ordering and anisotropic magnetoresistance in pseudo-single-crystal  $\gamma'$ -Fe<sub>4</sub>N films. *Appl. Phys. Express* **7**, 063003. (doi: 10.7567/APEX.7.063003)
- <sup>108</sup> Baltz V, Manchon A, Tsoi M, Moriyama T, Ono T, Tserkovnyak Y. 2018. Antiferromagnetic spintronics. *Rev. Mod. Phys.* **90**, 015005. (doi: 10.1103/RevModPhys.90.015005)
- <sup>109</sup> Wadley P *et al.* 2016. Electrical switching of an antiferromagnet. *Science* **351**, 6273. (doi:

10.1126/science.aab1031)

- <sup>110</sup> Zubáč J, Kašpar Z, Krizek F, Förster T, Campion RP, Novák V, Jungwirth T, Olejník K. Hysteretic effects and magnetotransport of electrically switched CuMnAs. *Phys. Rev. B* **104**, 184424. (doi: 10.1103/PhysRevB.104.184424)
- <sup>111</sup> Emmanouilidou E, Cao H, Tang P, Gui X, Hu C, Shen B, Wu J, Zhang S-C, Xie W, Ni N. 2017. Magnetic order induces symmetry breaking in the single-crystalline orthorhombic CuMnAs semimetal. *Phys. Rev. B* **96**, 224405. (doi: 10.1103/PhysRevB.96.224405)
- <sup>112</sup> Bodnar SY, Šmejkal L, Turek I, Jungwirth T, Gomonay O, Sinova J, Sapozhnik AA, Elmers H-J, Kläui M, Jourdan M. 2018. Writing and reading antiferromagnetic Mn<sub>2</sub>Au by Néel spin-orbit torques and large anisotropic magnetoresistance. *Nat. Commun.* **9**, 348. doi: 10.1038/s41467-017-02780-x
- <sup>113</sup> Manna K, Sun Y, Muechler L, Kübler J, Felser C. 2018. Heusler, Weyl and Berry. *Nature Reviews Materials* **3**, 244-256. (doi: 10.1038/s41578-018-0036-5)
- <sup>114</sup> Heusler F. 1903. Über magnetische Manganlegierungen. *Verhandlungen der Deutschen Physikalischen Gesellschaft* **5**, 219. (doi?)
- <sup>115</sup> Sakuraba Y, Kokado S, Hirayama Y, Furubayashi T, Sukegawa H, Li S, Takahashi YK, Hono K. 2014. Quantitative analysis of anisotropic magnetoresistance in Co<sub>2</sub>MnZ and Co<sub>2</sub>FeZ epitaxial thin films: A facile way to investigate spin-polarization in half-metallic Heusler compounds. *Appl. Phys. Lett.* **104**, 172407. (doi: 10.1063/1.4874851)
- <sup>116</sup> Yako H, Kubota T, Takanashi K. 2015. Anisotropic Magnetoresistance Effect in Co<sub>2</sub>(Fe–Mn)(Al–Si) Heusler Alloy Thin Film. *IEEE Trans Mag*, **51**, 11. (doi: 10.1109/TMAG.2015.2439284)
- <sup>117</sup> Oogane M, McFadden AP, Kota Y, Brown-Heft TL, Tsunoda M, Ando Y, Palmstrøm CJ. 2018. Fourfold symmetric anisotropic magnetoresistance in half-metallic Co<sub>2</sub>MnSi Heusler alloy thin films. *Jpn. J. Appl. Phys.* **57**, 063001. (doi: 10.7567/JJAP.57.063001)
- <sup>118</sup> Felser C, Hirohata A. 2016. Heusler alloys: Properties, Growth, Applications. Springer. (ISBN: 978-3-319-21449-8.)
- <sup>119</sup> Ciccarelli C *et al.* 2016. Room-temperature spin-orbit torque in NiMnSb. *Nature Phys.* **12**, 855. doi: 10.1038/nphys3772
- <sup>120</sup> Ohtomo A, Hwang HY. 2004. A high-mobility electron gas at the LaAlO<sub>3</sub>/SrTiO<sub>3</sub> heterointerface. *Nature* **427**, 423. (doi: 10.1038/nature02308)

- <sup>121</sup> Shalom MB, Tai CW, Lereah Y, Sachs M, Levy E, Rakhmilevitch D, Palevski A, Dagan Y. Anisotropic magnetotransport at the SrTiO<sub>3</sub>/LaAlO<sub>3</sub> interface. *Phys. Rev. B* **80**, 140403(R). (doi: 10.1103/PhysRevB.80.140403)
- <sup>122</sup> Reyren N *et al.* 2007. Superconducting Interfaces Between Insulating Oxides. *Science* **317**, 1196. (doi: 10.1126/science.1146006)
- <sup>123</sup> Huijben M, Brinkman A, Koster G, Rijnders G, Hilgenkamp H, Blank DHA. 2009. Structure–Property Relation of SrTiO<sub>3</sub>/LaAlO<sub>3</sub> Interfaces. *Adv. Mater.* **21**, 1665. (doi: 10.1002/adma.200801448)
- <sup>124</sup> Lebedev N, Stehno M, Rana A, Gauquelin N, Verbeeck J, Brinkman A, Aarts J. 2020. Inhomogeneous superconductivity and quasilinear magnetoresistance at amorphous LaTiO<sub>3</sub>/SrTiO<sub>3</sub> interfaces. *J. Phys.: Condens. Matter* **33**, 055001. (doi: 10.1088/1361-648X/abc102)
- <sup>125</sup> Boschker H, Mannhart J. 2017. Quantum-Matter Heterostructures. *Annu. Rev. Condens. Matter Phys.* **8**:145–64. (doi: 10.1146/annurev-conmatphys-031016-025404)
- <sup>126</sup> Bovenzi N, Diez M. 2017. Semiclassical theory of anisotropic transport at LaAlO<sub>3</sub>/SrTiO<sub>3</sub> interfaces under an in-plane magnetic field. *Phys. Rev. B* **95**, 205430. (doi: 10.1103/PhysRevB.95.205430)
- <sup>127</sup> Ariando, Wang X *et al.* 2011. Electronic phase separation at the LaAlO<sub>3</sub>/SrTiO<sub>3</sub> interface. *Nat. Commun.* **2**, 188. (doi: 10.1038/ncomms1192)
- <sup>128</sup> Rout PK, Agireen I, Maniv E, Goldstein M, Dagan Y. 2017. Six-fold crystalline anisotropic magnetoresistance in the (111) LaAlO<sub>3</sub>/SrTiO<sub>3</sub> oxide interface. *Phys. Rev. B* **95**, 241107(R). (doi: 10.1103/PhysRevB.95.241107)
- <sup>129</sup> Joshua A, Ruhman J, Pecker S, Altman E, Ilani S. 2013. Gate-tunable polarized phase of two-dimensional electrons at the LaAlO<sub>3</sub>/SrTiO<sub>3</sub> interface. *Proc. Natl. Acad. Sci. USA* **110**, 9633. (doi: 10.1073/pnas.1221453110)
- <sup>130</sup> Miao L, Du R, Yin Y, Li Q. 2016. Anisotropic magneto-transport properties of electron gases at SrTiO<sub>3</sub> (111) and (110) surfaces. *Appl. Phys. Lett.* **109**, 261604. (doi: 10.1063/1.4972985)
- <sup>131</sup> Harsan Ma HJ, Zhou J, Yang M, Liu Y, Zeng SW, Zhou WX, Zhang LC, Venkatesan T, Feng YP, Ariando. 2017. Giant crystalline anisotropic magnetoresistance in nonmagnetic perovskite oxide heterostructures. *Phys. Rev. B* **95**, 155314. (doi: 10.1103/PhysRevB.95.155314)
- <sup>132</sup> Boudjada N, Khait I, Paramekanti A. 2019. Anisotropic magnetoresistance in multiband systems: Two-dimensional electron gases and polar metals at oxide interfaces. *Phys. Rev. B* **99**,

195453. (doi: 10.1103/PhysRevB.99.195453)
- <sup>133</sup> Wadehra N, Tomar R, Varma RM, Gopal RK, Singh Y, Dattagupta S, Chakraverty S. 2020. Planar Hall effect and anisotropic magnetoresistance in polar-polar interface of LaVO<sub>3</sub>-KTaO<sub>3</sub> with strong spin-orbit coupling. *Nat. Commun.* **11**, 874. (doi: 10.1038/s41467-020-14689-z)
- <sup>134</sup> Tomar R, Kakkar S, Bera C, Chakraverty S. 2021. Anisotropic magnetoresistance and planar Hall effect in (001) and (111) LaVO<sub>3</sub> / SrTiO<sub>3</sub> heterostructures. *Phys. Rev. B* **103**, 115407. (doi: 10.1103/PhysRevB.103.115407)
- <sup>135</sup> Chen Y *et al.* 2015. Creation of High Mobility Two-Dimensional Electron Gases via Strain Induced Polarization at an Otherwise Nonpolar Complex Oxide Interface. *Nano Lett.* **15**, 1849. (doi: 10.1021/nl504622w)
- <sup>136</sup> Granada M, Bustingorry S, Pontello DE, Barturen M, Eddrief M, Marangolo M, Milano J. 2016. Magnetotransport properties of Fe<sub>0.8</sub>Ga<sub>0.2</sub> films with stripe domains. *Phys. Rev. B* **94**, 184435. (doi: 10.1103/PhysRevB.94.184435)
- <sup>137</sup> Jen SU. 1992. Anisotropic magnetoresistance of Co-Pd alloys. *Phys. Rev. B* **45**, 9819. (doi: 10.1103/PhysRevB.45.9819)
- <sup>138</sup> Philippi-Kobs A, Farhadi A, Matheis L, Lott D, Chuvilin A, Oepen HP. 2019. Impact of Symmetry on Anisotropic Magnetoresistance in Textured Ferromagnetic Thin Films. *Phys. Rev. Lett.* **123**, 137201. (doi: 10.1103/PhysRevLett.123.137201)
- <sup>139</sup> T. Hupfauer, A. Matos-Abiague, M. Gmitra, F. Schiller, J. Loher, D. Bougeard, C. H. Back, J. Fabian, and D. Weiss, Emergence of spin-orbit fields in magnetotransport of quasi-two-dimensional iron on gallium arsenide, *Nat. Commun.* **6**, 7374 (2015).
- <sup>140</sup> Shi X, Li X, Lai Z, Liu X, Mi W. 2020. Structure, magnetic and electronic transport properties in antiperovskite cubic  $\gamma'$ -CuFe<sub>3</sub>N polycrystalline films. *Intermetallics* **121**, 106779. (doi: 10.1016/j.intermet.2020.106779)
- <sup>141</sup> Tsunoda M, Komasaki Y, Kokado S, Isogami S, Chen C-C, Takahashi M. 2009. Negative Anisotropic Magnetoresistance in Fe<sub>4</sub>N Film. *Appl. Phys. Express* **2**, 083001. (doi: 10.1143/APEX.2.083001)
- <sup>142</sup> Tsunoda M, Takahashi H, Kokado S, Komasaki Y, Sakuma A, Takahashi M. 2010. Anomalous Anisotropic Magnetoresistance in Pseudo-Single-Crystal  $\gamma'$ -Fe<sub>4</sub>N Films. *Appl. Phys. Express* **3**, 113003. (doi: 10.1143/APEX.3.113003)
- <sup>143</sup> Klein L, Marshall AF, Reiner JW, Ahn CH, Geballe TH, Beasley MR, Kapitulnik A. 1998.

- Large magnetoresistance of single-crystal films of ferromagnetic SrRuO<sub>3</sub>. *J. Magn. Magn. Mater.* **188**, 319. (doi: 10.1016/S0304-8853(98)00201-7)
- <sup>144</sup> Herranz G, Sanchez F, Garcia-Cuenca MV, Ferrater C, Varela M, Martinez B; Fontcuberta J. 2004. Anisotropic magnetoresistance in SrRuO<sub>3</sub> ferromagnetic oxide. *J. Magn. Magn. Mater.* **272-276**, 517. (doi: 10.1016/j.jmmm.2003.12.1050)
- <sup>145</sup> Rao RA, Kacedon DB, Eom CB. 1998. Anisotropic magnetotransport properties of epitaxial thin films of conductive ferromagnetic oxide SrRuO<sub>3</sub>. *J. Appl. Phys.* **83**, 6995. (doi: 10.1063/1.367674)
- <sup>146</sup> Haham N, Shperber Y, Reiner JW, Klein L. 2013. Low-temperature anisotropic magnetoresistance and planar Hall effect in SrRuO<sub>3</sub>. *Phys. Rev. B.* **87**, 144407. (doi: 10.1103/PhysRevB.87.144407)
- <sup>147</sup> Chaurasia R, Asokan K, Kumar K, Pramanik AK. 2021. Low-temperature ferromagnetism in perovskite SrIrO<sub>3</sub> films. *Phys. Rev. B* **103**, 064418. (doi: 10.1103/PhysRevB.103.064418)
- <sup>148</sup> Zeng Z, Greenblatt M, and Croft M. 1999. Large magnetoresistance in antiferromagnetic CaMnO<sub>3-δ</sub>. *Phys. Rev. B* **59**, 8784. (doi: 10.1103/PhysRevB.59.8784)
- <sup>149</sup> Li X *et al.* 2021. Charge Disproportionation and Complex Magnetism in a PbMnO<sub>3</sub> Perovskite Synthesized under High Pressure. *Chem. Mater.* **33**, 1, 92–101. (doi: 10.1021/acs.chemmater.0c02706)
- <sup>150</sup> Bibes M, Laukhin V, Valencia S, Martinez B, Fontcuberta J, Gorbenko OY, Kaul AR, Martinez JL. 2005. Anisotropic magnetoresistance and anomalous Hall effect in manganite thin films. *J. Phys.: Condens. Matter* **17** 2733. (doi: <http://dx.doi.org/10.1088/0953-8984/17/17/022>)
- <sup>151</sup> O'Donnell J, Eckstein JN, Rzechowski MS. 2000. Temperature and magnetic field dependent transport anisotropies in La<sub>0.7</sub>Ca<sub>0.3</sub>MnO<sub>3</sub> films. *Appl. Phys. Lett.* **76**, 218. (<https://doi.org/10.1063/1.125707>)
- <sup>152</sup> Yang S, Chen Q, Yang Y, Gao Y, Xu R, Zhang H, Ma J. 2021. Silver addition in polycrystalline La<sub>0.7</sub>Ca<sub>0.3</sub>MnO<sub>3</sub>: Large magnetoresistance and anisotropic magnetoresistance for manganite sensors. *J. Alloys Compd.* **882**, 160719. (doi: 10.1016/j.jallcom.2021.160719)
- <sup>153</sup> Sharma H, Tulapurkar A, Tomy CV. 2014. Sign reversal of anisotropic magnetoresistance in La<sub>0.7</sub>Ca<sub>0.3</sub>MnO<sub>3</sub>/SrTiO<sub>3</sub> ultrathin films. *Appl. Phys. Lett.* **105**, 222406. (doi: 10.1063/1.4903236)
- <sup>154</sup> Xie Y, Yang H, Liu Y, Yang Z, Chen B, Zuo Z, Katlakunta S, Zhan Q, Li R-W. 2013. Strain

- induced tunable anisotropic magnetoresistance in  $\text{La}_{0.67}\text{Ca}_{0.33}\text{MnO}_3/\text{BaTiO}_3$  heterostructures. *J Appl Phys* **113**, 17C716. (doi: 10.1063/1.4795841)
- <sup>155</sup> Kandpal LM, Singh S, Kumar P, Siwach PK, Gupta A, Awana VPS, Singh HK. 2016. Magnetic anisotropy and anisotropic magnetoresistance in strongly phase separated manganite thin films. *J. Magn. Magn. Mater.* **408**, 60. (doi: 10.1016/j.jmmm.2016.02.022)
- <sup>156</sup> Egilmez M, Saber MM, Mansour AI, Ma R, Chow KH, Jung J. 2008. Dramatic strain induced modification of the low field anisotropic magnetoresistance in ultrathin manganite films. *Appl. Phys. Lett.* **93**, 182505. (doi: 10.1063/1.3021083)
- <sup>157</sup> Wong AT, Beekman C, Guo H, Siemons W, Gai Z, Arenholz E, Takamura Y, Ward TZ. 2014. Strain driven anisotropic magnetoresistance in antiferromagnetic  $\text{La}_{0.4}\text{Sr}_{0.6}\text{MnO}_3$ . *Appl. Phys. Lett.* **105**, 052401. (doi: 10.1063/1.4892420)
- <sup>158</sup> Infante IC, Laukhin V, Sanchez F, Fotcuberta J, Melnikov O, Gorbenko OY, Kaul AR. 2006. Anisotropic magnetoresistance in epitaxial (110) manganite films. *J. Appl. Phys.* **99**, 08C502. (<https://doi.org/10.1063/1.2150812>)
- <sup>159</sup> Kumar P, Prasad R, Dwivedi RK, Singh HK. 2011. Out-of-plane low field anisotropic magnetoresistance in  $\text{Nd}_{0.51}\text{Sr}_{0.49}\text{MnO}_3$  thin films. *J. Magn. Magn. Mater.* **323**, 2564. (doi: 10.1016/j.jmmm.2011.05.032)
- <sup>160</sup> Chen YZ, Sun JR, Zhao TY, Wang J, Wang ZH, Shen BG, Pryds N. 2009. Crossover of angular dependent magnetoresistance with the metal-insulator transition in colossal magnetoresistive manganite films. *Appl. Phys. Lett.* **95**, 132506. (doi: 10.1063/1.3240407)
- <sup>161</sup> Li P, Jin C, Jiang EY, Bai HL. 2010. Origin of the twofold and fourfold symmetric anisotropic magnetoresistance in epitaxial. *J. Appl. Phys.* **108**, 093921. (doi: 10.1063/1.3499696)
- <sup>162</sup> Bai H *et al.* 2022. Observation of Spin Splitting Torque in a Collinear Antiferromagnet  $\text{RuO}_2$ . *Phys. Rev. Lett.* **128**, 197202. (doi: 10.1103/PhysRevLett.128.197202)
- <sup>163</sup> Fang D, Kurebayashi H, Wunderlich J, Výborný K, Zarbo LP, Campion RP, Casiraghi A, Gallagher BL, Jungwirth T, Ferguson AJ. 2011. Spin-orbit-driven ferromagnetic resonance. *Nature Nanotech.* **6**, 413. (doi: 10.1038/nnano.2011.68)
- <sup>164</sup> Mellnik AR, Lee JS, Richardella A, Grab JL, Mintun PJ, Fischer MH, Vaezi A, Manchon A, Kim E-A, Samarth N, Ralph DC. 2014. Spin-transfer torque generated by a topological insulator. *Nature* **511**, 449. (doi: 10.1038/nature13534)
- <sup>165</sup> Booth K, Gray I, Dahlberg ED. 2021. Determining the AC susceptibility of thin metal

- films using the anisotropic magnetoresistance. *J. Magn. Magn. Mater.* **523**, 167631. (doi: 10.1016/j.jmmm.2020.167631)
- <sup>166</sup> Pignard S, Goglio G, Radulescu A, Piraux L, Dubois S, Declémy A, Duvail JL. 2002. Study of the magnetization reversal in individual nickel nanowires. *J. Appl. Phys.* **87**, 824. (doi: 10.1063/1.371947)
- <sup>167</sup> Wegrowe J-E, Kelly D, Franck A, Gilbert SE, Ansermet J-Ph. 1999. Magnetoresistance of Ferromagnetic Nanowires. *Phys. Rev. Lett.* **82**, 3681. (doi: 10.1103/PhysRevLett.82.3681.)
- <sup>168</sup> Rheem Y, Yoo B-Y, Beyermann WP, Myung NV. 2006. Magnetotransport studies of a single nickel nanowire. *Nanotechnology* **18**, 015202. (doi: 10.1088/0957-4484/18/1/015202)
- <sup>169</sup> Hayashi M, Thomas L, Rettner C, Moriya R, Jiang X, Parkin SP. 2006. Dependence of Current and Field Driven Depinning of Domain Walls on Their Structure and Chirality in Permalloy Nanowires. *Phys. Rev. Lett.* **97**, 207205. (doi: 10.1103/PhysRevLett.97.207205)
- <sup>170</sup> Nam Hai P, Duc Anh L, Tanaka M. 2012. Electron effective mass in n-type electron-induced ferromagnetic semiconductor (In,Fe)As: Evidence of conduction band transport. *Appl. Phys. Lett.* **101**, 252410. (doi: 10.1063/1.4772630)
- <sup>171</sup> Campbell IA, Fert A, Jaoul O. 1970. The spontaneous resistivity anisotropy in Ni-based alloys. *J. Phys. C* **3**, S95. (doi: 10.1088/0022-3719/3/1S/310)
- <sup>172</sup> Berger L. 2011. Spin relaxation in metallic ferromagnets. *Phys. Rev. B* **83**, 054410. (doi: 10.1103/PhysRevB.83.054410)
- <sup>173</sup> Narayanapillai K, Gopinadhan K, Qiu X, Annadi A, Ariando, Venkatesan T, Yang H. 2014. Current-driven spin orbit field in LaAlO<sub>3</sub>/SrTiO<sub>3</sub> heterostructures. *Appl. Phys. Lett.* **105**, 162405. (doi: 10.1063/1.4899122)
- <sup>174</sup> Feng Z *et al.* 2012. Spin Hall angle quantification from spin pumping and microwave photoresistance. *Phys. Rev. B* **85**, 214423. (doi: 10.1103/PhysRevB.85.214423)
- <sup>175</sup> Mosendz O, Pearson JE, Fradin FY, Bauer GEW, Bader SD, Hoffmann A. 2010. Quantifying Spin Hall Angles from Spin Pumping: Experiments and Theory. *Phys. Rev. Lett.* **104**, 046601. (doi: 10.1103/PhysRevLett.104.046601)
- <sup>176</sup> Xing X, Xu C, Li Z, Feng J, Zhou N, Zhang Y, Sun Y, Zhou W, Xu X, Sh Z. 2018. Angular-dependent magnetoresistance study in Ca<sub>0.73</sub>La<sub>0.27</sub>FeAs<sub>2</sub>: a ‘parent’ compound of 112-type iron pnictide superconductors. *J. Phys.: Condens. Matter* **30**, 025701. (doi: 10.1088/1361-648X/aa9c11)

- <sup>177</sup> Park J-H, Ko H-W, Kim J-M, Park J, Park S-Y, Jo Y, Park B-G, Kim SK, Lee K-J, Kim K-J. 2021. Temperature dependence of intrinsic and extrinsic contributions to anisotropic magnetoresistance. *Sci. Rep.* **11**, 20884. (doi: 10.1038/s41598-021-00374-8)
- <sup>178</sup> Tesařová N *et al.* 2014. Systematic study of magnetic linear dichroism and birefringence in (Ga,Mn)As. *Phys. Rev. B* **89**, 085203. (doi: 10.1103/PhysRevB.89.085203)
- <sup>179</sup> Silber R *et al.* 2019. Quadratic magneto-optic Kerr effect spectroscopy of Fe epitaxial films on MgO(001) substrates. *Phys. Rev. B* **100**, 064403. (doi: 10.1103/PhysRevB.100.064403)
- <sup>180</sup> Hamrle J, Blomeier S, Gaier O, Hillebrands B, Schneider H, Jakob G, Postava K, Felser C. 2007. Huge quadratic magneto-optical Kerr effect and magnetization reversal in the Co<sub>2</sub>FeSi Heusler compound. *J. Phys. D: Appl. Phys.* **40**, 1563. doi: 10.1088/0022-3727/40/6/S09
- <sup>181</sup> Valencia S, Kleibert A, Gaupp A, Ruzs J, Legut D, Bansmann J, Gudat W, Oppeneer PM. 2010. Quadratic X-Ray Magneto-Optical Effect upon Reflection in a Near-Normal-Incidence Configuration at the M Edges of 3d-Transition Metals. *Phys. Rev. Lett.* **104**, 187401. doi: 10.1103/PhysRevLett.104.187401
- <sup>182</sup> Zink BL. 2022. Thermal effects in spintronic materials and devices: An experimentalist's guide. *J. Magn. Magn. Mater.* **564**, 170120. (doi: 10.1016/j.jmmm.2022.170120)
- <sup>183</sup> Slachter A, Bakker FL, van Wees BJ. 2011. Modeling of thermal spin transport and spin-orbit effects in ferromagnetic/nonmagnetic mesoscopic devices. *Phys. Rev. B* **84**, 174408. (doi: 10.1103/PhysRevB.84.174408)
- <sup>184</sup> Wegrowe J-E, Drouhin H-J, Lacour D. 2014. Anisotropic magnetothermal transport and spin Seebeck effect. *Phys. Rev. B* **89**, 094409. (doi: 10.1103/PhysRevB.89.094409)
- <sup>185</sup> Jungwirth T, Wunderlich J, Novák V, Olejník K, Gallagher BL, Campion RP, Edmonds KW, Rushforth AW, Ferguson AJ, Němec P. 2014. Spin-dependent phenomena and device concepts explored in (Ga,Mn)As. *Rev. Mod. Phys.* **86**, 855. (doi: 10.1103/RevModPhys.86.855)
- <sup>186</sup> Kimling J, Gooth J, Nielsch K. 2013. Anisotropic magnetothermal resistance in Ni nanowires. *Phys. Rev. B* **87**, 094409. (doi: 10.1103/PhysRevB.87.094409)
- <sup>187</sup> Heikkilä TT, Hatami M, Bauer GEW. 2010. Spin heat accumulation and its relaxation in spin valves. *Phys. Rev. B* **81**, 100408(R). (doi: 10.1103/PhysRevB.81.100408)
- <sup>188</sup> Corliss LM, Elliott N, Hastings JM, Sass RL. 1961. Magnetic Structure of Chromium Selenide. *Phys. Rev.* **122**, 1402. (doi: 10.1103/PhysRev.122.1402)
- <sup>189</sup> Shindou R, Nagaosa N. 2001. Orbital Ferromagnetism and Anomalous Hall Effect in Anti-

- ferromagnets on the Distorted fcc Lattice. *Phys. Rev. Lett.* **87**, 116801. (doi: 10.1103/PhysRevLett.87.116801)
- <sup>190</sup> Chen H, Niu Q, MacDonald AH. 2014. Anomalous Hall Effect Arising from Noncollinear Antiferromagnetism. *Phys. Rev. Lett.* **112**, 017205. (doi: 10.1103/PhysRevLett.112.017205)
- <sup>191</sup> Velez J, Sabirianov RF, Jaswal SS, Tsymbal EY. 2005. Ballistic Anisotropic Magnetoresistance. *Phys. Rev. Lett.* **94**, 127203. (doi: 10.1103/PhysRevLett.94.127203)
- <sup>192</sup> Hu C, Teng J, Yu G, Lu W, Ji W. 2015. Conditions for quantized anisotropic magnetoresistance. *Phys. Rev. B* **91**, 045438. (doi: 10.1103/PhysRevB.91.045438)
- <sup>193</sup> Autès G, Barreteau C, Spanjaard D, Desjonquères M-C. 2008. Electronic transport in iron atomic contacts: From the infinite wire to realistic geometries. *Phys. Rev. B* **77**, 155437. (doi: 10.1103/PhysRevB.77.155437)
- <sup>194</sup> Moodera JS, Kinder LR, Wong TM, Meservey R. 1995. Large Magnetoresistance at Room Temperature in Ferromagnetic Thin Film Tunnel Junctions. *Phys. Rev. Lett.* **74**, 3273. (doi: 10.1103/PhysRevLett.74.3273)
- <sup>195</sup> Julliere M. 1975. Tunneling between ferromagnetic films. *Phys. Lett. A* **54**, 225. (doi: 10.1016/0375-9601(75)90174-7)
- <sup>196</sup> Gould C, Rüster C, Jungwirth T, Girgis E, Schott GM, Giraud R, Brunner K, Schmidt G, Molenkamp LW. 2004. Tunneling Anisotropic Magnetoresistance: A Spin-Valve-Like Tunnel Magnetoresistance Using a Single Magnetic Layer. *Phys. Rev. Lett.* **93**, 117203. (doi: 10.1103/PhysRevLett.93.117203)
- <sup>197</sup> Schöneberg J, Ferriani P, Heinze S, Weismann A, Berndt R. 2018. Tunneling anisotropic magnetoresistance via molecular  $\pi$  orbitals of Pb dimers. *Phys. Rev. B* **97**, 041114. (doi: 10.1103/PhysRevB.97.041114)
- <sup>198</sup> Kandala A, Richardella A, Kempinger S, Liu C-X, Samarth N. 2015. Giant anisotropic magnetoresistance in a quantum anomalous Hall insulator. *Nat. Commun.* **6**, 7434, (doi: 10.1038/ncomms8434)
- <sup>199</sup> Heidecker J. 2013. MRAM Technology Status. JPL Publication 13-3. [cited 2022 Nov 11] Available from: <https://ntrs.nasa.gov/api/citations/20140000668/downloads/20140000668.pdf>
- <sup>200</sup> Bartok A, Daniel L, Razek A. 2013. A multiscale model for thin film AMR sensors. *J. Magn. Mater.* **326**, 116. (doi: 10.1016/j.jmmm.2012.08.020)

- <sup>201</sup> Stutzke NA, Russek SE, Pappas DP, Tondra M. 2005. Low-frequency noise measurements on commercial magnetoresistive magnetic field sensors. *J. Appl. Phys.* **97**, 10Q107. (doi: 10.1063/1.1861375)
- <sup>202</sup> Honeywell. Magnetic Displacement Sensors. Technical Report HMC 1501-1512. [cited 2022 Nov 11] Available from: [https://aerospace.honeywell.com/content/dam/aerobt/en/documents/learn/products/sensors/datasheet/N61-2042-000-000\\_MDS\\_HMC15011512-ds.pdf](https://aerospace.honeywell.com/content/dam/aerobt/en/documents/learn/products/sensors/datasheet/N61-2042-000-000_MDS_HMC15011512-ds.pdf)
- <sup>203</sup> Philips Semiconductors. 2000. Application Note, General Magnetoresistive Sensors for Magnetic Field Measurement, Technical Report KMZ10. [cited 2022 Nov 11] Available from: [https://www.mikrocontroller.net/attachment/27041/SC17\\_GENERAL\\_MAG\\_2-1.pdf](https://www.mikrocontroller.net/attachment/27041/SC17_GENERAL_MAG_2-1.pdf)
- <sup>204</sup> Adelerhof DJ, Geven W. 2000. New position detectors based on AMR sensors. *Sens. Actuator A Phys.* **85**, 48. (doi: 10.1016/S0924-4247(00)00341-1)
- <sup>205</sup> Včelak J, Ripka P, Kubik J, Platil A, Kašpar P. 2005. AMR navigation systems and methods of their calibration. *Sens. Actuator A Phys.* **123-124**, 122. (doi: 10.1016/j.sna.2005.02.040)
- <sup>206</sup> Mlejnek P, Vopalensky M, Ripka P. 2008. AMR current measurement device. *Sens. Actuator A Phys.* **141**, 649. (doi: 10.1016/j.sna.2007.10.016)
- <sup>207</sup> Schuhl A, Van Dau FN, Childress JR. 1995. Low-field magnetic sensors based on the planar Hall effect. *Appl. Phys. Lett.* **66**, 2751. (doi: 10.1063/1.113697)
- <sup>208</sup> Jungwirth T, Niu Q, MacDonald AH. 2002. Anomalous Hall Effect in Ferromagnetic Semiconductors. *Phys. Rev. Lett.* **88**, 207208. (doi: 10.1103/PhysRevLett.88.207208)
- <sup>209</sup> Breidenbach AT, Yu H, Peterson TA, McFadden AP, Peria WK, Palmstrøm CJ, Crowell PA. 2022. Anomalous Nernst and Seebeck coefficients in epitaxial thin film  $\text{Co}_2\text{MnAl}_x\text{Si}_{1-x}$  and  $\text{Co}_2\text{FeAl}$ . *Phys. Rev. B* **105**, 144405. (doi: 10.1103/PhysRevB.105.144405)
- <sup>210</sup> Note that even if all  $\rho_{ii}$  components are equal in a cubic crystal when  $\vec{M} = 0$ , additional crystalline AMR terms appear (unlike for polycrystals) once magnetisation is taken into account.